Revealing the precipitation behavior of crack-free TiB_2/Al-Zn-Mg-Cu composites manufactured by Laser Powder Bed Fusion

Guichuan Li [a*], Bensu Tunca [a], Seren Senol [a], Massimiliano Casata [a], Yi Wu [b], Zhe Chen [b], Kim Vanmeensel [a*]

[a]*KU Leuven, Department of Materials Engineering, Kasteelpark Arenberg 44 - 3001 Leuven, Belgium*
[b]*State Key Laboratory of Metal Matrix Composites, Shanghai Jiao Tong University, Shanghai, 200240, PR China*
***Corresponding authors**: Guichuan Li, email: guichuan.li@kuleuven.be*
Kim Vanmeensel, email: kim.vanmeensel@kuleuven.be

Abstract

The microstructural evolution and precipitation behavior in additively manufactured age-hardenable TiB_2/Al-Zn-Mg-Cu composites were investigated. As-built (AB), direct-aged (DA), solution-treated, and T6 heat-treated samples were characterized at macro, micro, and nano-scales to provide fundamental insights on the effect of the non-equilibrium L-PBF solidification microstructure and the presence of TiB_2 reinforcement particles on the precipitation behavior. Crack-free and near fully dense (99.7%) TiB_2/Al-Zn-Mg-Cu composites were successfully manufactured using L-PBF. The composites exhibited a fine equiaxed microstructure containing nanometer- and submicrometer-sized TiB_2 particles, possessing an improved hardness compared to unreinforced Al-Zn-Mg-Cu alloys. The heterogeneous chemistry and the heterogeneously distributed dislocation density, both direct consequences of the rapid L-PBF solidification, were preserved in the DA sample. The resulting non-uniform distribution of η' precipitates led to a hardness of 200 ± 5 HV, showing a 40 HV increase compared to the AB sample. A solution heat treatment enabled the dissolution of interdendritic segregated elements in the AB sample, resulting in a chemically homogeneous FCC-Al matrix. Simultaneously, it decreased the dislocation density and induced the formation of needle-shaped Al_7Cu_2Fe phases. The subsequent ageing treatment promoted a high density of well-dispersed η' nanoprecipitates, leading to an overall Vickers hardness of 215 ± 2 HV for the T6 sample. The TiB_2/Al-Zn-Mg-Cu composite exhibited an accelerated precipitation behavior compared to the unmodified Al-Zn-Mg-Cu alloy, attributed to a higher solute content, enhanced grain boundary segregation resulting from increased high-angle grain boundaries, heterogeneous precipitation at the TiB_2/Al interfaces, and on the thermal expansion mismatch dislocations in the vicinity of the TiB_2 particles.

Keywords: Additive manufacturing; Laser Powder Bed Fusion; Aluminum alloy; Metal matrix composite; Hot cracking; Precipitation

1. Introduction

Laser Powder Bed Fusion (L-PBF) Additive Manufacturing (AM) has been recognized as a revolutionary manufacturing technique capable of fabricating near-net-shaped three-dimensional (3D) metallic components with intricate geometries and advanced performance for aerospace, medical, and automotive applications [1–4]. The L-PBF-processed alloys usually show intrinsically unique microstructures due to the rapid solidification characteristics and complex cyclic thermal history, distinct from their counterparts fabricated using traditional casting or wrought techniques [2,5,6]. The ultra-high cooling rate (10^5-10^6 K/s) of L-PBF results in non-equilibrium microstructures with fine microstructural features and supersaturated metal matrix [4,7,8], which offers great strengthening potential for age-hardenable alloys such as Al-Zn-Mg-based aluminum alloy [9,10], Cu-Cr-based copper alloy [11,12], and Hastelloy X alloy [13]. The high temperature gradient, directional heat extraction, and localized heating/cooling cycles during L-PBF create high-density dislocations in the as-built materials [14,15]. These unique microstructure features could profoundly affect the strength-ductility synergy of the as-built materials and the precipitation behavior upon post-heat treatments [16–18]. However, attempts on the adaptation of age-hardenable aluminum alloys, such as Al-Cu-Mg and Al-Zn-Mg-based alloys, that have been mainly developed for the traditional wrought process to L-PBF usually encounter severe hot cracking problems [9,19,20]. This consequently impedes the further applications of L-PBF in industries [16]. Therefore, the development of alternative alloys with compositions tailored specifically for L-PBF has scientific and economic significance.

Recently, aluminum-based Metal Matrix Composites (MMCs) have attracted increasing interest in AM industries due to their good processability and excellent mechanical performance [21–26]. For example, Li. et al. reported on the fabrication of nano-TiB_2 reinforced AlSi10Mg alloy using L-PBF, exhibiting an excellent combination of tensile strength ~530 MPa and ductility ~15.5% [21]. Ghoncheh et al. demonstrated a new generation additively manufactured TiB_2-inoculated Al-Cu-Mg-Ag alloy, named A205 alloy, consisting of a fully equiaxed ultra-fine grain structure [22]. The L-PBF-fabricated parts were crack-free and exhibited isotropic mechanical properties, showing a tensile strength ~281MPa and an excellent ductility ~19.4% of the horizontally and vertically sectioned samples [22]. Gu et al. successfully incorporated nano and micrometer-sized TiC and SiC particles in the AlSi10Mg alloy [23]. The high densification level and homogeneous dispersion of the reinforcement particles in the L-PBF-fabricated MMCs ensured a good tensile strength ~486 MPa without degrading the ductility ~10.8% [23]. Other examples could include TiN [24], LaB_6 [25], and boron-doped TiC [26] reinforced aluminum-based MMCs. Advances in powder metallurgy and traditional metal shaping techniques showed that the presence of reinforcing particles plays a crucial role in the precipitation kinetics and the concomitant synergistic strengthening effect of reinforcing particles and precipitates [27–31]. However, investigations on the effect of reinforcing particles on the precipitation behavior of additively manufactured aluminum-based MMCs, particularly for the age-hardenable aluminum alloys, are rather limited.

In age-hardenable aluminum-based MMCs, the physical properties of reinforcing particles and particle Al interface structure could significantly affect the precipitation behavior [27–31]. For example, Wang et al. reported that the SiC/Al interfaces showed an increased dislocation density induced by thermoelastic stresses due to the mismatch of thermal expansion coefficient between the SiC particles and the Al matrix, which accelerated the precipitation of $Al_5Cu_2Mn_3$ and θ' phase in an extruded SiC-reinforced Al-Cu-Mg-based MMC [27]. In addition, Strangwood et al. reported that interfacial segregation of Zn, Mg, and Cu as well as heterogeneous precipitation were observed on the SiC/Al interfaces, alongside the presence of precipitate-free-zones (PFZs) in the adjacent matrix in the under-aged samples [28]. Besides, the precipitate characteristics were closely related to the heat treatment

FOR THE PUBLISHED MANUSCRIPT, PLEASE VISIT ***ADDITIVE MANUFACTURING***: HTTPS://DOI.ORG/10.1016/J.ADDMA.2023.103460

conditions [28]. Ma et al. revealed the preferential heterogeneous nucleation of $(Zn_{1.5}Cu_{0.5})Mg$ phase on the TiB_2/Al interface in an extruded composite with the absence of thermoelastic stress induced dislocations [29]. The reduced nucleation energy barrier and the presence of highly dense misfit dislocations at the semi-coherent TiB_2/Al interfaces promoted the nucleation and growth of the precipitates [29]. In a B_4C-reinforced Al-Zn-Mg-based MMC synthesized by powder metallurgy, the presence of coarse η'/η precipitates associated with PFZs was observed near the B_4C/Al interfaces, while the fine precipitates were homogeneously distributed in the matrix [30]. Interfacial reaction at the B_4C/Al interface could occur during powder metallurgy at temperatures above 620 °C, resulting in the formation of Al_3BC and MgB_2 at the interface [31]. The interfacial segregation of Cu further enhanced the nucleation rate of precipitates at the interface [31]. Consequently, the particle/matrix interface structure, solute segregation, precipitate characteristics, and the presence of PFZs could significantly affect the corrosion, quasi-static and dynamic material properties [10,32,33].

The objective of the present work is to provide fundamental insights into the effect of reinforcing particles on the precipitation behavior of additively manufactured age-hardenable aluminum-based MMCs, comparing the direct-aged (DA), solution-treated (ST), and T6 state. In this context, a TiB_2/Al-Zn-Mg-Cu composite powder synthesized using an in-situ mixed salt method followed by gas atomization was used for L-PBF. The investigation from macro-, micro-, and nano-scales aims to elucidate the following contents: (1) the effect of non-equilibrium microstructural characteristics in materials solidified under the L-PBF condition on the precipitation behavior of aluminum-based MMC; (2) the effect of reinforcing particles on the precipitation behavior of the composite, investigating the general precipitation behaviors in the bulk materials and the heterogeneous precipitation behavior on the particle/matrix interfaces and near the reinforcing particles. The present work on tailoring the precipitation behavior and microstructure evolution during heat treatment could provide fundamental inputs to render mechanical properties of additively manufactured aluminum-based MMC.

2. Materials and experimental methods

2.1. Feedstock powder fabrication

In this study, a TiB_2/Al-Zn-Mg-Cu composite powder with 3.43 vol% (~5.41 wt%) TiB_2 was designed for L-PBF. Additional Zn and Mg, as compared to the chemical composition designation of AA7075, were introduced in the starting powder to compensate for their losses due to evaporation during the L-PBF process. The TiB_2/Al-Zn-Mg-Cu composite was synthesized using an in-situ molten metal-salts (K_2TiF_6 and KBF_4) reaction method at 900 °C in an electrical resistance furnace [29]. The molten material was then cast into a graphite mold after slag removal. Subsequently, the TiB_2/Al-Zn-Mg-Cu composite powder was produced in a closed-coupled atomizer using an argon gas [21]. The fabrication route of TiB_2-reinforced composite powders has been described more in detail in earlier work [34]. The chemical composition analyzed at Element Materials Technology (USA) using inductively coupled plasma optical emission spectroscopy (ICP-OES) is given in Table 1.

Table 1. Chemical composition (wt%), relative density, and crack fraction of the feedstock powders and the L-PBF processed alloys.

Materials		Al	Zn	Mg	Cu	Fe	Ti	B	Rel. den.	Crack den.
Al-Zn-Mg-Cu	powder	Bal.	5.62	2.02	1.64	0.16	< 0.01	< 0.01	N/A	N/A
TiB_2/Al-Zn-Mg-Cu	powder	Bal.	8.42	2.57	1.88	0.42	3.98	1.80	N/A	N/A
Al-Zn-Mg-Cu	As-built	Bal.	4.63	1.75	1.64	0.16	< 0.01	< 0.01	96.3 ± 0.7%	3.3 ± 0.7%
TiB_2/Al-Zn-Mg-Cu	As-built	Bal.	6.48	2.27	2.01	0.44	3.73	1.68	99.7 ± 0.1%	0%

FOR THE PUBLISHED MANUSCRIPT, PLEASE VISIT ***ADDITIVE MANUFACTURING***: HTTPS://DOI.ORG/10.1016/J.ADDMA.2023.103460

The TiB_2/Al-Zn-Mg-Cu powder with a D10, D50, and D90 of 13, 30, and 45 µm, respectively, was used for the L-PBF experiments. Fig. 1 presents the morphology and cross-sectional microstructure of the TiB_2/Al-Zn-Mg-Cu composite powder, revealing a spherical morphology. Satellite particles are frequently observed. The cross-sectional SEM image and the corresponding EDS elemental maps of an individual powder show an equiaxed microstructure with submicrometer- and nanometer-sized TiB_2 particles pre-existing in the feedstock powder. A commercially available virgin Al-Zn-Mg-Cu (AA7075) gas-atomized powder supplied by LPW technology Ltd. (UK) was used as a reference material.

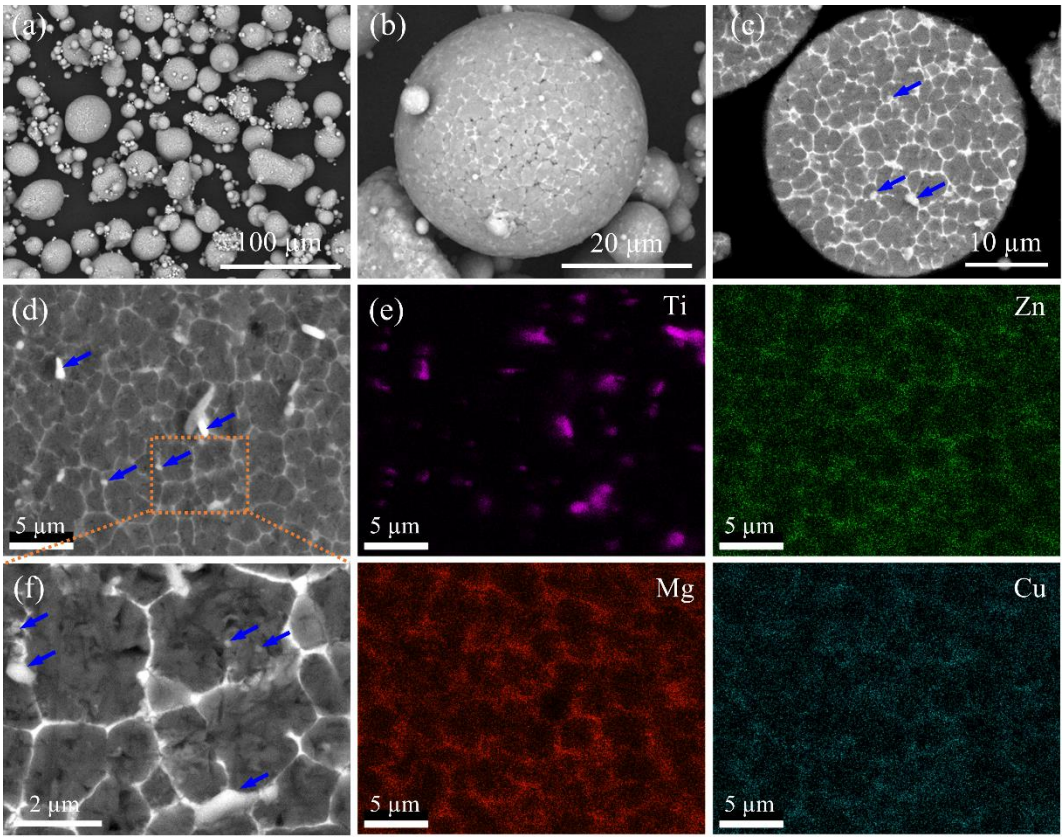

Fig. 1. SEM images of (a) overall morphology, (b) particle surface, and (c) cross-section of the TiB_2/Al-Zn-Mg-Cu powder, (d) cross-section of an individual TiB_2/Al-Zn-Mg-Cu powder particle with (e) corresponding EDS elemental maps of Ti, Zn, Mg, and Cu. (f) BSE-SEM micrograph at a higher magnification of the selected area in (d). The powder is mostly spherical, yet containing attached satellite particles. Submicrometer- and nanometer-sized TiB_2 particles are embedded within the gas-atomized powders. The blue arrows pointing to the TiB_2 particles.

2.2. Laser-based powder bed fusion process

Both the virgin Al-Zn-Mg-Cu alloy and the TiB_2/Al-Zn-Mg-Cu composite were manufactured in a 3D Systems Prox DMP 200 machine equipped with a 1070 nm fiber laser, with a laser beam size of 70 µm and a maximum laser power of 300 W. During the L-PBF process, the building chamber was filled with argon to maintain a minimized oxygen level. The optimized laser parameter settings were: laser power of 270 W, scanning speed of 500 mm/s, hatch spacing of 105 µm, layer thickness of 30 µm. A bi-directional scanning strategy with 90° rotation between the successive layers was applied. The optimized parameter set was utilized to fabricate all the samples in the present work. Table 1 summarizes the chemical composition (wt%) of both feedstock powders and as-built (AB) parts. Moreover, the relative density (%) and crack fraction (%) of the AB parts processed both feedstock powders is reported. The relative density and crack fraction were determined using image analysis in

FOR THE PUBLISHED MANUSCRIPT, PLEASE VISIT ***ADDITIVE MANUFACTURING***: HTTPS://DOI.ORG/10.1016/J.ADDMA.2023.103460

ImageJ. At least three images each covering an area of 1.5 × 1.5 mm² were utilized. As indicated in Table 1, the Zn and Mg losses experienced during L-PBF are 17.6 and 13.4 wt% for the Al-Zn-Mg-Cu alloy and 23.0 and 11.7 wt% for the TiB_2/Al-Zn-Mg-Cu composite, respectively.

2.3. Heat treatment

To investigate the precipitation behavior of the L-PBF processed alloys, direct ageing (DA) and T6 heat treatments were conducted. Specifically, during the DA heat treatment, the as-built (AB) samples were artificially aged at 120 °C for maximum 24 h, followed by air cooling. During the T6 heat treatment, the as-built samples were firstly solution treated (ST) at 470 °C for 2 h, followed by water quenching. Subsequently, the ST samples were subjected to artificial ageing at 120 °C for maximum 24 h and air cooled to room temperature. Vicker's microhardness tests were conducted to evaluate the hardness response of the samples subjected to heat treatments.

2.4. Materials characterization

Differential scanning calorimetry (DSC) (TA Instruments TA 2920) was employed to study the kinetic response of both alloys. DSC curves were obtained for the 25 – 700 °C temperature range at a scan rate of 10 °C/min in an argon atmosphere. For microstructural characterization, samples were grinded and polished according to the standard metallographic procedure. Optical macrographs were obtained in a Keyence VHX6000 microscope. Scanning Electron Microscopy (SEM) and Transmission Electron Microscopy (TEM) were used to characterize the microstructural features of the AB and heat-treated samples. The DA and T6 samples were subjected to an ageing treatment at 120 °C for 24 h. A FEI-Nova NanoSEM 450 instrument equipped with a back-scatter detector (BSE) and an electron backscatter diffraction (EBSD) detector was used for microstructure and grain orientation characterization. During the grain orientation mapping, a scan area of 500 × 500 µm² with a step size of 1 µm and a scan area of 120 × 120 µm² with a step size of 0.1 µm were used for the virgin Al-Zn-Mg-Cu and TiB_2/Al-Zn-Mg-Cu alloys, respectively. The accelerating voltage was fixed at 20 kV. Thin foil samples for TEM examinations were prepared using a dual beam microscope (Focused Ion Beam, FIB, Nova NanoLab 600 DualBeam, FEI) following a standard lift-out procedure [35], using 30 kV Ga ions for milling and final 2 kV Ga ions for final cleaning. High-resolution TEM (HRTEM) and scanning TEM (STEM) images, fast Fourier transformation (FFT) patterns, selected area electron diffraction (SAED) patterns, and energy dispersive spectrometry (EDS) mappings were collected using TEM/STEM (JEOL ARM200F). High-angle annular dark field (HAADF) and annular bright field (ABF) detectors were used for STEM imaging.

3. Results

3.1. Characterization of L-PBF-processed samples

The structural features of the L-PBF processed alloys were characterized at the macro-, micro-, and nano-scales using OM, SEM, and TEM.

3.1.1. Macro-scale structure

Fig. 2 presents the optical macrographs of the Al-Zn-Mg-Cu alloy and TiB_2/Al-Zn-Mg-Cu composite manufactured by L-PBF, showing vastly different L-PBF processibility and part quality. A substantial amount of cracks is observed in the as-built Al-Zn-Mg-Cu alloy, indicating a severe hot cracking problem during L-PBF. The X-Z and Y-Z views reveal that the long cracks are mainly parallel to the building direction (Z coordinate) and spanning over multiple melt pool layers, while the X-Y view shows an interconnected crack network. The presence of hot cracks and remaining pores in the Al-Zn-Mg-Cu alloy results in a poor part continuity with an overall low relative density of 96.3 ± 0.7%, with

FOR THE PUBLISHED MANUSCRIPT, PLEASE VISIT ***ADDITIVE MANUFACTURING***: HTTPS://DOI.ORG/10.1016/J.ADDMA.2023.103460

3.3 ± 0.7% of cracks, as listed in Table 1. In contrast, the TiB_2/Al-Zn-Mg-Cu composite is crack-free and achieves a high relative density of 99.7 ± 0.1% (Table 1), revealing the effectiveness of TiB_2 particles in eliminating the hot cracks.

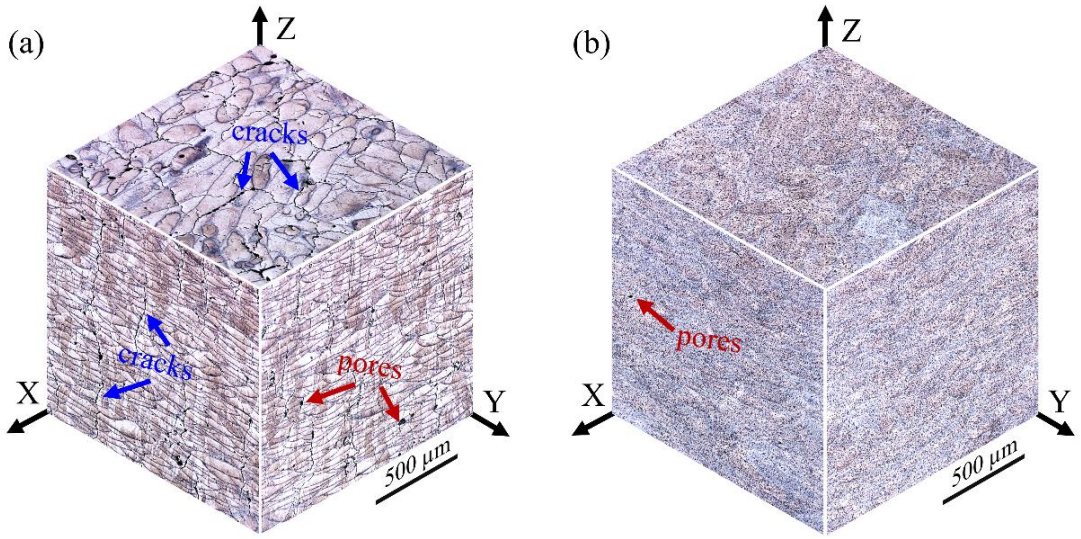

Fig. 2. Isometric 3D views showing the macrostructure of (a) Al-Zn-Mg-Cu and (b) TiB_2/Al-Zn-Mg-Cu L-PBF processed samples, with the building direction parallel to the z coordinate. A substantial amount of cracks is present in the Al-Zn-Mg-Cu sample. In contrast, the TiB_2/Al-Zn-Mg-Cu sample is free of cracks. Both samples contain a small amount of residual pores.

3.1.2. Micro-scale structure

The EBSD orientation maps in Fig. 3 demonstrate a remarkable difference in the grain morphology, grain size, and crystallographic orientation of the L-PBF fabricated Al-Zn-Mg-Cu alloy and TiB_2/Al-Zn-Mg-Cu composite, as recorded in the XZ plane. Fig. 3a reveals a coarse columnar grain morphology in the as-built Al-Zn-Mg-Cu sample, growing epitaxially across multiple successive deposition layers and parallel to the building direction (Z coordinate). The columnar grains show a width ranging from 5 to 90 μm and a length up to a few hundred micrometers. As a result, a strong (001) texture with a maximum texture index of 7.5 is present along the building direction (Fig. 3c), due to the directional solidification as a consequence of the steep temperature gradient during the L-PBF solidification process and the lack of potential nucleants [7,20,36,37]. In addition, a considerable amount of hot cracks can be observed in the as-built Al-Zn-Mg-Cu sample, mainly propagating along the columnar grain boundaries and parallel to the building direction. On the contrary, Figs. 3b and d show that the TiB_2/Al-Zn-Mg-Cu composite exhibits a uniform fine equiaxed microstructure with a low texture index of 1.6, featured as a nearly random crystallographic texture. The grain size distributions in Figs. 3e and f illustrate that a significantly refined grain structure with an average grain size of 2.0 ± 0.9 μm is achieved in the TiB_2/Al-Zn-Mg-Cu composite, compared to an average grain size of 53.3 ± 28.2 μm for the Al-Zn-Mg-Cu alloy. This confirms the excellent grain refinement effect and heterogeneous nucleation efficiency of TiB_2 for Al grains. Moreover, the fraction of high angle grain boundaries (HAGBs), which are defined as grain boundaries with a misorientation angle larger than 15°, slightly increases from 64.5% for the Al-Zn-Mg-Cu alloy to 69.7% for the TiB_2/Al-Zn-Mg-Cu composite.

FOR THE PUBLISHED MANUSCRIPT, PLEASE VISIT ***ADDITIVE MANUFACTURING***: HTTPS://DOI.ORG/10.1016/J.ADDMA.2023.103460

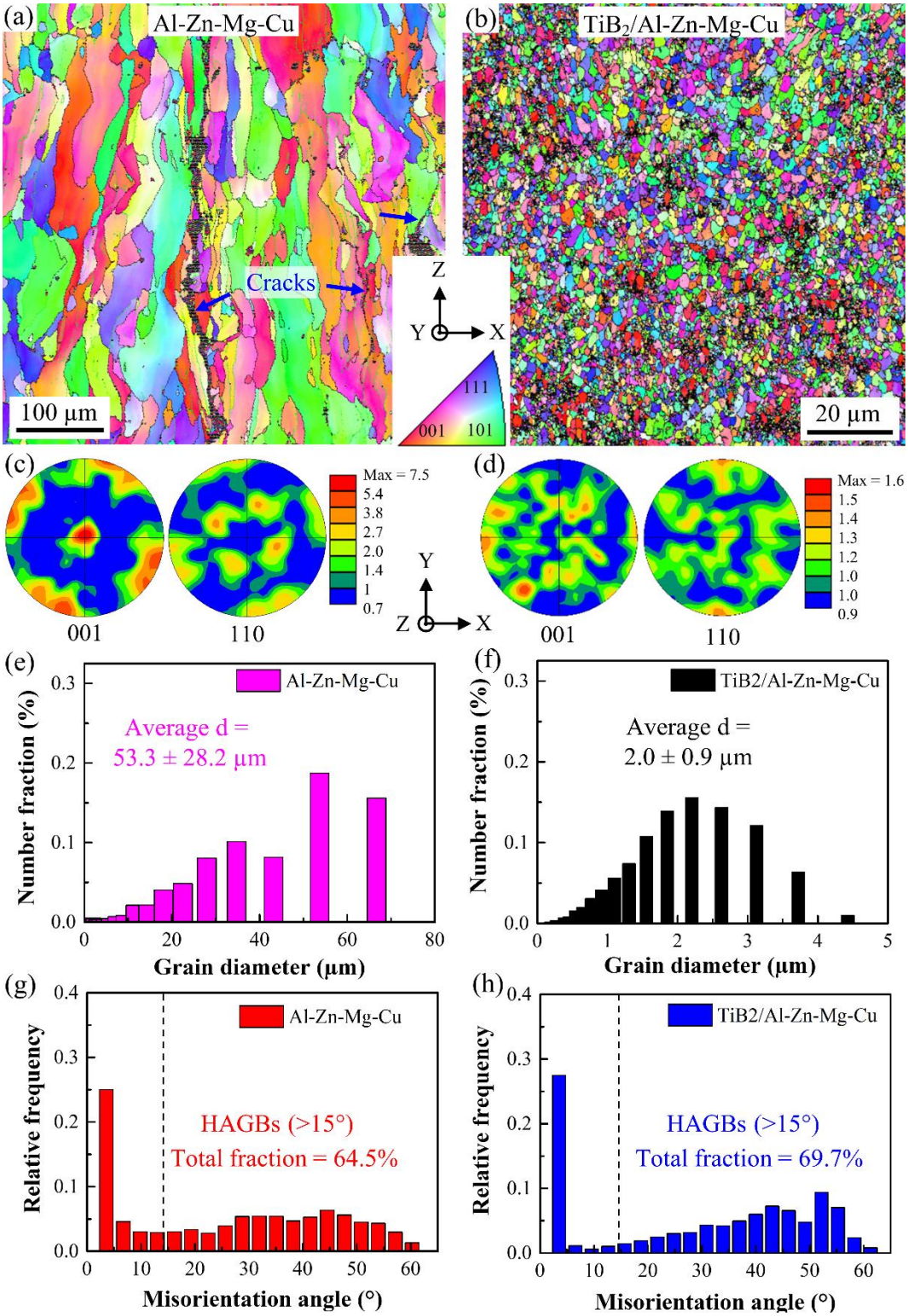

Fig. 3. EBSD orientation maps and corresponding (001) (110) pole figures of the L-PBF fabricated (a, c) Al-Zn-Mg-Cu and (b, d) TiB_2/Al-Zn-Mg-Cu samples. Note that the scale bars in the two orientation maps are different. Hot cracks in (a) are indicated by the blue arrows. High angle grain boundaries (HAGBs) with a misorientation angle larger than 15° are shown in black, while low angle grain boundaries (LAGBs) with a misorientation angle smaller than 15° are drawn in green. Grain size distribution and misorientation angle distribution of (e, g) Al-Zn-Mg-Cu and (f, h) TiB_2/Al-Zn-Mg-Cu samples, measured from the corresponding orientation maps shown in (a, b). The building direction is parallel to the Z direction.

FOR THE PUBLISHED MANUSCRIPT, PLEASE VISIT ***ADDITIVE MANUFACTURING***: HTTPS://DOI.ORG/10.1016/J.ADDMA.2023.103460

3.1.3. *Micro- to nano-scale structure*

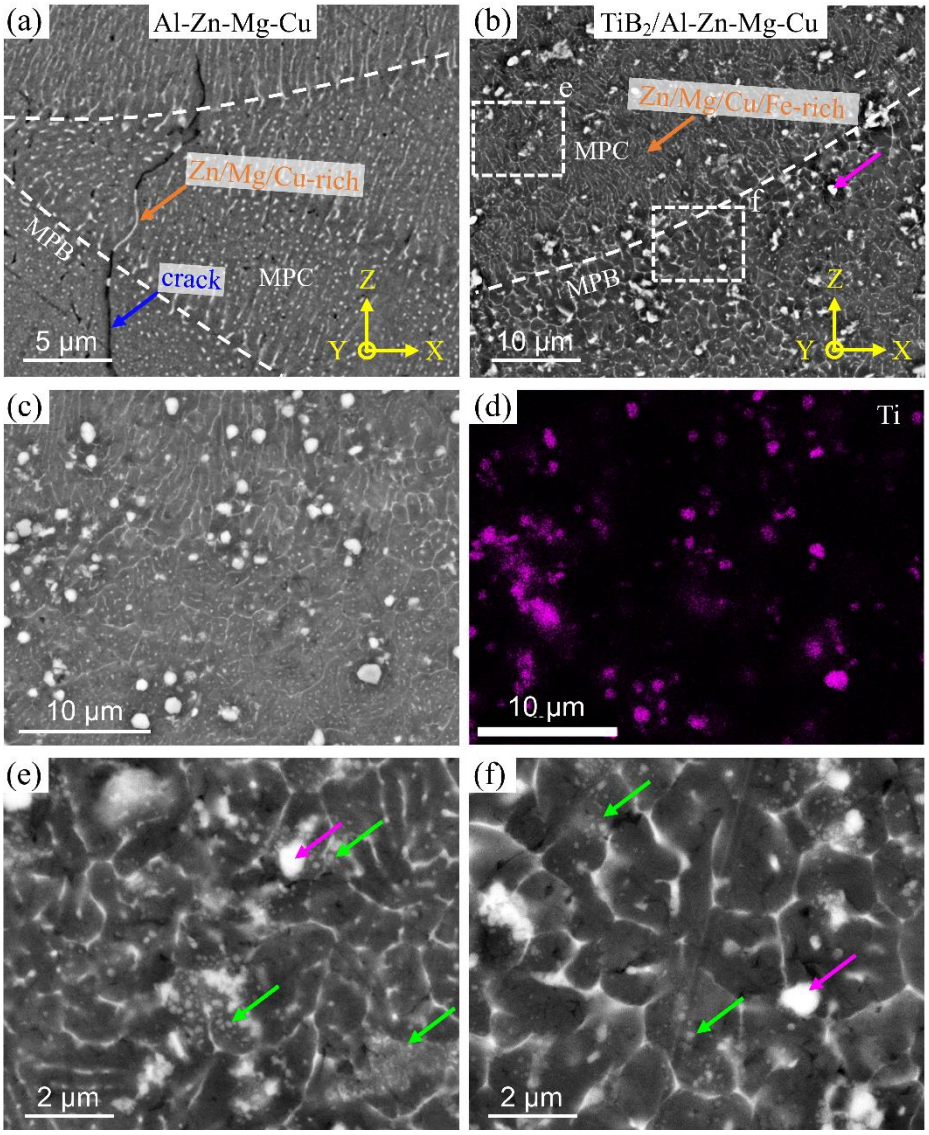

Fig. 4. BSE-SEM images of the L-PBF processed (a) Al-Zn-Mg-Cu and (b-f) TiB_2/Al-Zn-Mg-Cu samples under the as-built (AB) condition. (c) BSE-SEM image and (d) the corresponding EDS elemental mapping of Ti show the distribution of TiB_2 in the matrix. The marked melt pool center (MPC) and melt pool boundary (MPB) regions in (b) are presented in (e) and (f), respectively. Pink arrows point to the submicrometer-sized TiB_2 particles mainly at the dendritic boundaries. Green arrows point to the nanometer-sized TiB_2 particles at the dendritic boundaries and in the grain interiors. Agglomeration of TiB_2 particles, especially the nanometer-sized particles, can be observed.

The microstructures of L-PBF processed Al-Zn-Mg-Cu and TiB_2/Al-Zn-Mg-Cu alloys are compared using BSE-SEM, as shown in Fig. 4. The Al-Zn-Mg-Cu alloy (Fig. 4a) shows a dominant columnar dendritic subgrain structure with Zn/Mg/Cu-rich eutectic phases (bright phase) located at the interdendritic regions. It is noteworthy that a grain boundary that is partially decorated with eutectic phases (the bright phase) develops into a crack due to the poor interdendritic liquid back-filling during solidification, which is a typical feature of hot cracks [9,38,39]. Whereas, the TiB_2/Al-Zn-Mg-Cu composite (Figs. 4b) exhibits an equiaxed dendritic morphology with segregation of Zn, Mg, Cu, and Fe (bright network) in the interdendritic regions. Around 0.44 wt% of Fe is presented as impurity element in the TiB_2/Al-Zn-Mg-Cu composite, as suggested by the chemical analysis in Table 1. The BSE-SEM image in Fig. 4c and the corresponding EDS map of Ti reveal the distribution of TiB_2 in

FOR THE PUBLISHED MANUSCRIPT, PLEASE VISIT ***ADDITIVE MANUFACTURING***: HTTPS://DOI.ORG/10.1016/J.ADDMA.2023.103460

the as-built TiB_2/Al-Zn-Mg-Cu sample. SEM micrographs at higher magnification (Figs. 4e and f) show that the melt pool center has a slightly finer dendritic microstructure compared to the melt pool boundary due to a higher cooling rate [4]. Similar to the gas-atomized TiB_2/Al-Zn-Mg-Cu powder (Fig. 1), submicrometer and nanometer-sized TiB_2 particles are observed in the as-built sample. The pink arrows indicate that the submicrometer-sized TiB_2 particles are mainly located at the dendritic boundaries. As indicated by the green arrows, the nanometer-sized particles present both at the dendritic boundaries and within the Al grains, with agglomeration readily observed. The TiB_2 phase has good thermal stability in Al with a melting temperature of ~3004 K, as predicted by Thermo-Calc. The thermodynamic simulation results are presented in supplementary Fig. S-1. Most TiB_2 particles that pre-existed in the gas-atomized powders, especially the submicrometer-sized ones (Fig. 1), can be preserved after the L-PBF process. Partial melting of TiB_2 particles during the L-PBF processing is possible due to the high temperature experienced in the melt pool [40]. It is noticed that an increased amount of nanometer-sized TiB_2 particles is observed in the as-built part (Figs. 4e and f) compared to that in the gas-atomized powder (Fig. 1). This could be related to the partial melting of TiB_2 particles that pre-existed in the gas-atomized powders and re-precipitation during the L-PBF process.

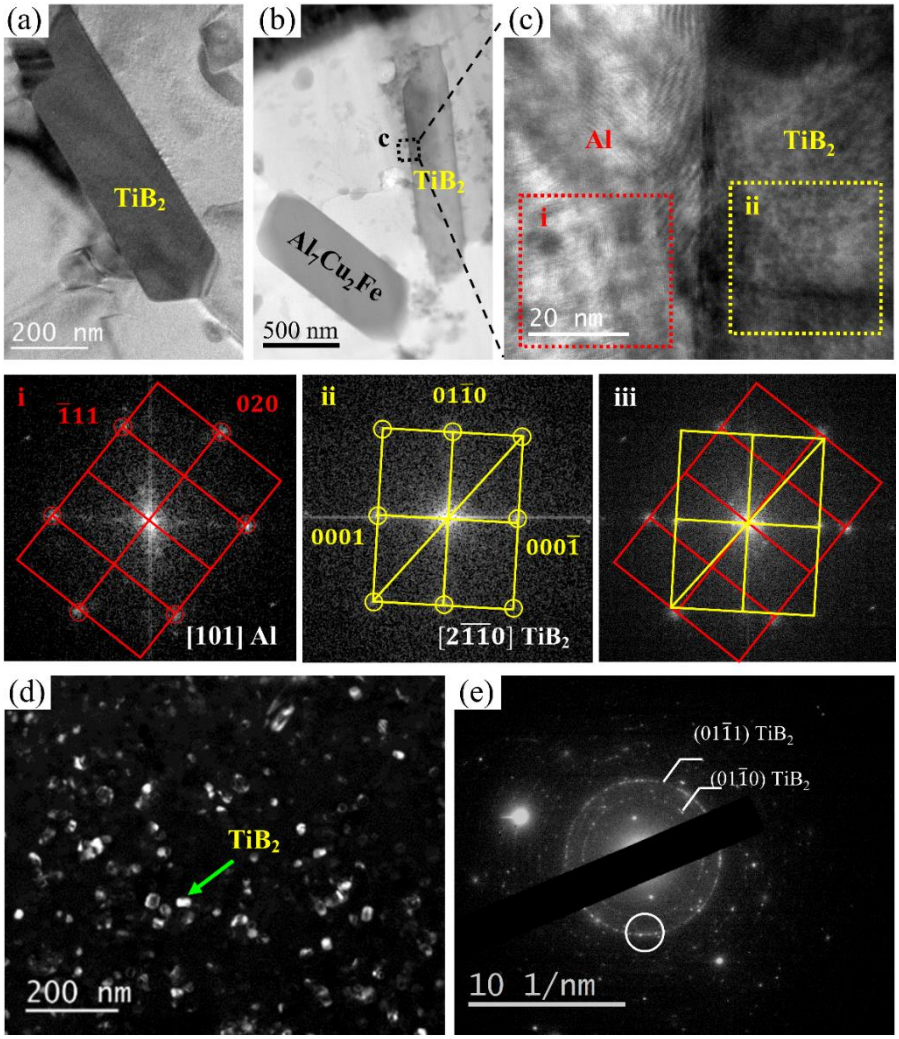

Fig. 5. (a) BF-STEM and (b) ABF-STEM images showing the hexagonal-shaped submicrometer-sized TiB_2 particles. (c) High-resolution STEM image of the Al/TiB_2 interface from (b), with the corresponding fast Fourier transformation (FFT) patterns from the selected area of the Al matrix and TiB_2 shown in (i) and (ii), respectively. (iii) The corresponding FFT pattern of (c) showing the OR between TiB_2 and Al. (d) DF-STEM image showing the distribution of nanometer-sized TiB_2 particles in the grain interior. (e) The circle in the SAED pattern indicates the objective aperture position used for forming the DF image in (d).

FOR THE PUBLISHED MANUSCRIPT, PLEASE VISIT ***ADDITIVE MANUFACTURING***: HTTPS://DOI.ORG/10.1016/J.ADDMA.2023.103460

To better reveal the morphology of TiB_2 particles, the solution-treated and T6 TiB_2/Al-Zn-Mg-Cu samples were used for TEM observation so that the microsegregation in the as-built solidification microstructure could be removed. The bright field (BF) and annular bright field (ABF) STEM images in Figs. 5a and b show a hexagonal morphology of the submicrometer-sized TiB_2 particles. The high-resolution TEM (HRTEM) image of the interface between a submicrometer-sized TiB_2 particle and the Al matrix is given in Fig. 5c. The associated fast Fourier transformation (FFT) patterns in Figs. 4i-iii show a good crystallographic lattice match between the TiB_2 particle and the neighboring Al grain. A crystallographic orientation relationship (OR) of $[2\bar{1}\bar{1}0]_{TiB2}//[101]_{Al}$ and $(0001)_{TiB2}//(11\bar{1})_{Al}$, with an angle of around 3° between the $(01\bar{1}1)_{TiB2}$ and $(020)_{Al}$, and 3° between the $(0\bar{1}12)_{TiB2}$ and $(\bar{2}02)_{Al}$ is identified, indicating a semi-coherent interface. This OR-Al/TiB_2 can be found for the submicrometer-sized hexagonal-shaped TiB_2 particles at the grain boundaries and in the grain interiors, which is reported to be the most favorable OR between Al/TiB_2 with the lowest lattice misfit and interfacial energy [21,29,34]. The dark field (DF)-STEM image in Fig. 5d shows the agglomeration of nanometer-sized granular-shaped TiB_2 particles within an individual Al grain, using the objective aperture position indicated by the circle in the SAED pattern (Fig. 5e). These nanometer-sized TiB_2 particles have an average particle size of ~ 40 nm. Moreover, these agglomerated nanometer-sized TiB_2 particles do not have specific crystallographic orientation relationships with the Al matrix, showing random orientations as suggested by the ring-shaped SAED patterns.

3.2. Heat treatment response of the L-PBF-processed samples

3.2.1. Hardness evolution during heat treatment

Fig. 6 presents the hardness variations versus holding time during direct ageing (DA) and conventional T6 heat treatments for the LPBF processed Al-Zn-Mg-Cu and TiB_2/Al-Zn-Mg-Cu alloys. Compared to the virgin Al-Zn-Mg-Cu alloy, the TiB_2/Al-Zn-Mg-Cu composite shows an overall higher hardness in all heat treatment conditions, for instance, 163 ± 6 HV compared to 97 ± 7 HV in AB condition. During the DA heat treatment, as shown in Fig. 6a, the hardness of both alloys continuously increases, indicating that the L-PBF process allows a certain amount of alloying element supersaturation available for precipitate formation. A maximum hardness value of 133 ± 2 and 200 ± 5 HV is reached after ageing at 120 °C for 24h for the Al-Zn-Mg-Cu alloy and TiB_2/Al-Zn-Mg-Cu composite, respectively. Fig. 6b shows that the hardness value of both AB alloys increases during the solutionizing step, labeled as solution treatment (ST), of the T6 heat treatment, resulting in a hardness value of 118 ± 12 and 171 ± 3 HV for the Al-Zn-Mg-Cu and TiB_2/Al-Zn-Mg-Cu alloy, respectively. Moreover, the subsequent ageing heat treatment further improves the hardness to a peak value of 166 ± 2 HV for the Al-Zn-Mg-Cu alloy and 215 ± 2 HV for the TiB_2/Al-Zn-Mg-Cu alloy, which is higher than that of the DA sample. The results indicate that a ST is beneficial for promoting the precipitation hardening effect of the L-PBF processed Al-Zn-Mg-Cu-based alloys prior to an ageing heat treatment. The L-PBF-processed and T6 heat-treated TiB_2/Al-Zn-Mg-Cu composites show a superior hardness than the L-PBF-processed Al-Mn-Sc alloys after peak aged at 300 °C for 5h (186 ± 4 HV) [5], the Zr/Sc/Hf-modified Al-Mn-Mg alloy after peak aged at 325 °C for 10h (173 ± 4 HV) [18], and the ZrH_2-inoculanted 7075 alloy (around 150 HV) [20].

FOR THE PUBLISHED MANUSCRIPT, PLEASE VISIT ***ADDITIVE MANUFACTURING***: HTTPS://DOI.ORG/10.1016/J.ADDMA.2023.103460

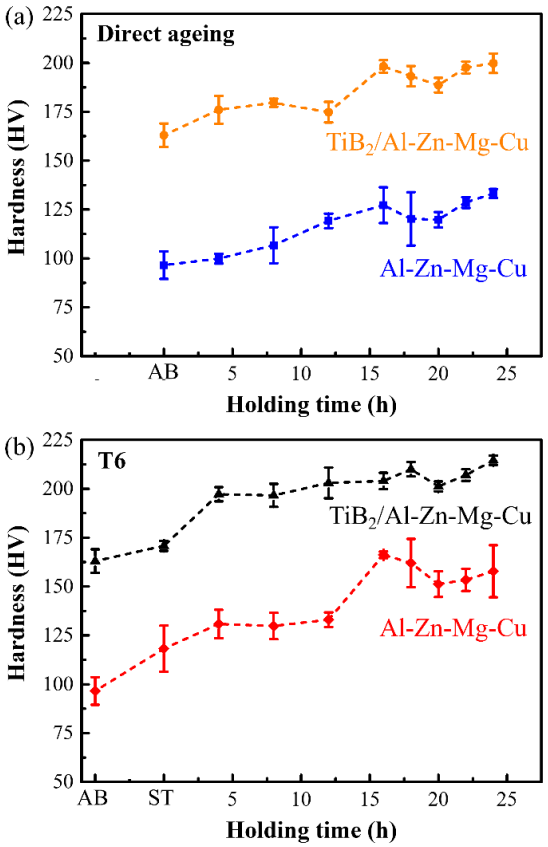

Fig. 6. Hardness evolution of L-PBF processed Al-Zn-Mg-Cu and TiB_2/Al-Zn-Mg-Cu alloys at different holding time during (a) DA and (b) T6 heat treatment.

3.2.2. Micro-scale structure of the heat-treated samples

The microstructures of the Al-Zn-Mg-Cu and TiB_2/Al-Zn-Mg-Cu alloys under AB, DA, ST, and T6 conditions are compared using BSE-SEM. Figs. 7 a, e, and i present the dendritic microstructure of the as-built samples, as previously shown in Fig. 4. Figs. 7b, f and j show that the DA samples of both alloys preserve the as-built solidification microstructural features, revealing predominant interdendritic microsegregation and distinguishable melt pool tracks. From Figs. 7c and g, the disappearance of melt pool borders and the dissolution of alloying elements that segregated in the interdendritic regions in both Al-Zn-Mg-Cu and TiB_2/Al-Zn-Mg-Cu alloys are clearly observed after the solution treatment (ST). As such, a supersaturated FCC-Al solid solution is obtained. Unlike the Al-Zn-Mg-Cu alloy, which displays a nearly segregation-free Al matrix in the ST state, the ST TiB_2/Al-Zn-Mg-Cu alloy contains a high amount of particles in the Al matrix. In addition to the TiB_2 particles, the precipitation of a uniformly distributed needle-shaped intermetallic phase is evident in the TiB_2/Al-Zn-Mg-Cu alloy, as indicated by the yellow arrows in Figs. 7g and k. A detailed analysis on the needle-shaped intermetallic phase will be presented in Fig. 13 in section 3.3.2, confirming that they are Al_7Cu_2Fe intermetallic phases. The T6 samples in Figs. 7d, h and l show an identical microstructure as the corresponding ST samples. The morphology and size of the needle-shaped Al_7Cu_2Fe intermetallic phase in ST and T6 TiB_2/Al-Zn-Mg-Cu samples are similar, showing an average width and length of 0.14 ± 0.03, 1.11 ± 0.43 µm for the ST sample and 0.15 ± 0.03, 1.15 ± 0.38 µm for the T6 sample, respectively. In addition, submicrometer- and nanometer-sized TiB_2 particles are observed in all the TiB_2/Al-Zn-Mg-Cu samples and their morphology and distribution remain unchanged after all the heat treatments, confirming their excellent thermal stability.

FOR THE PUBLISHED MANUSCRIPT, PLEASE VISIT ***ADDITIVE MANUFACTURING***: HTTPS://DOI.ORG/10.1016/J.ADDMA.2023.103460

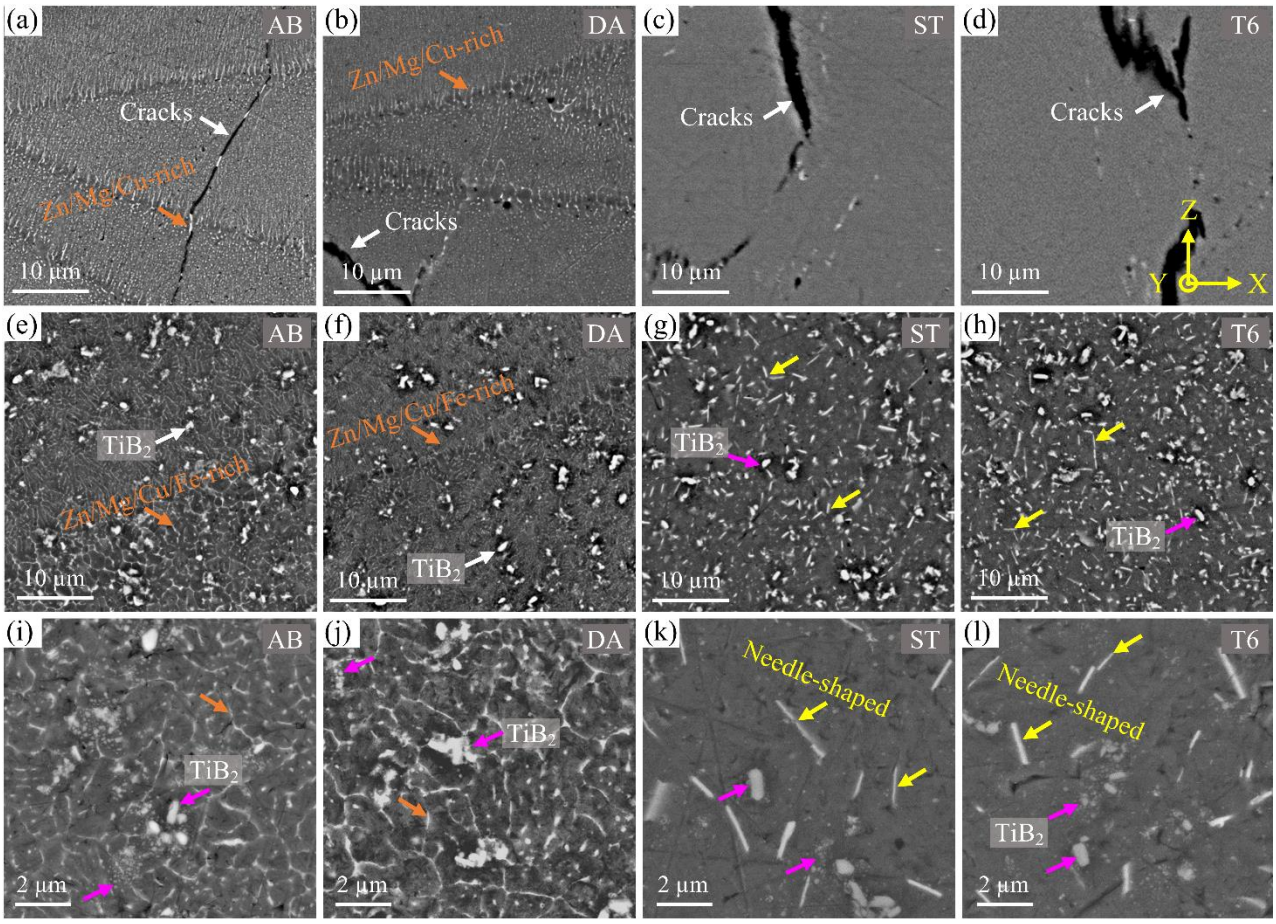

Fig. 7. BSE-SEM images of (a-d) Al-Zn-Mg-Cu alloy and (e-l) TiB_2/Al-Zn-Mg-Cu composite under AB, DA, ST, and T6 conditions comparing their microstructural features. (i-l) BSE-SEM images of TiB_2/Al-Zn-Mg-Cu composite at higher magnification.

The microstructures of heat-treated TiB_2/Al-Zn-Mg-Cu composite samples are further analyzed using TEM. ABF-STEM images in Figs. 8 a, c, and e compare the microstructural features such as dislocations and secondary phases under DA, ST, and T6 conditions. For the DA sample, a large amount of dislocations is present at the dendritic boundaries and in the dendrite interiors. In contrast, the amount of dislocations in the ST and T6 samples is significantly lower. It suggests that the high dislocation density in the DA sample originates from the rapid solidification process during L-PBF and is preserved after the ageing heat treatment. Moreover, the HAADF-STEM images and the corresponding elemental EDS maps in Figs. 8b, d, and f show a substantial difference among the microstructural features and elemental distribution in these three samples. The DA sample exhibits a profound heterogeneous chemistry. Profound segregation of Zn, Mg, Cu, and Fe in the interdendritic regions, including at the HAGBs, and a gradient concentration within the FCC-Al matrix can be observed, related to the solidification dendritic feature observed in Fig. 7. Interdendritic segregation of alloying elements has disappeared in the ST sample, resulting in a homogeneous distribution of Zn, Mg, and Cu in the Al matrix. Most of the Fe combines with Al and Cu forming a coarse elongated intermetallic phase, which corresponds to the needle-shaped phases observed in Figs. 7k and l. After T6, the depletion of Zn and Mg in the vicinity of HAGBs is noticeable. Nevertheless, the Zn, Mg, and Cu are dispersed homogeneously in the Al matrix. It is worth noticing that some TiB_2 particles are coinciding with the enrichment of Zn, Mg, and Cu under all heat treatment conditions.

FOR THE PUBLISHED MANUSCRIPT, PLEASE VISIT ***ADDITIVE MANUFACTURING***: HTTPS://DOI.ORG/10.1016/J.ADDMA.2023.103460

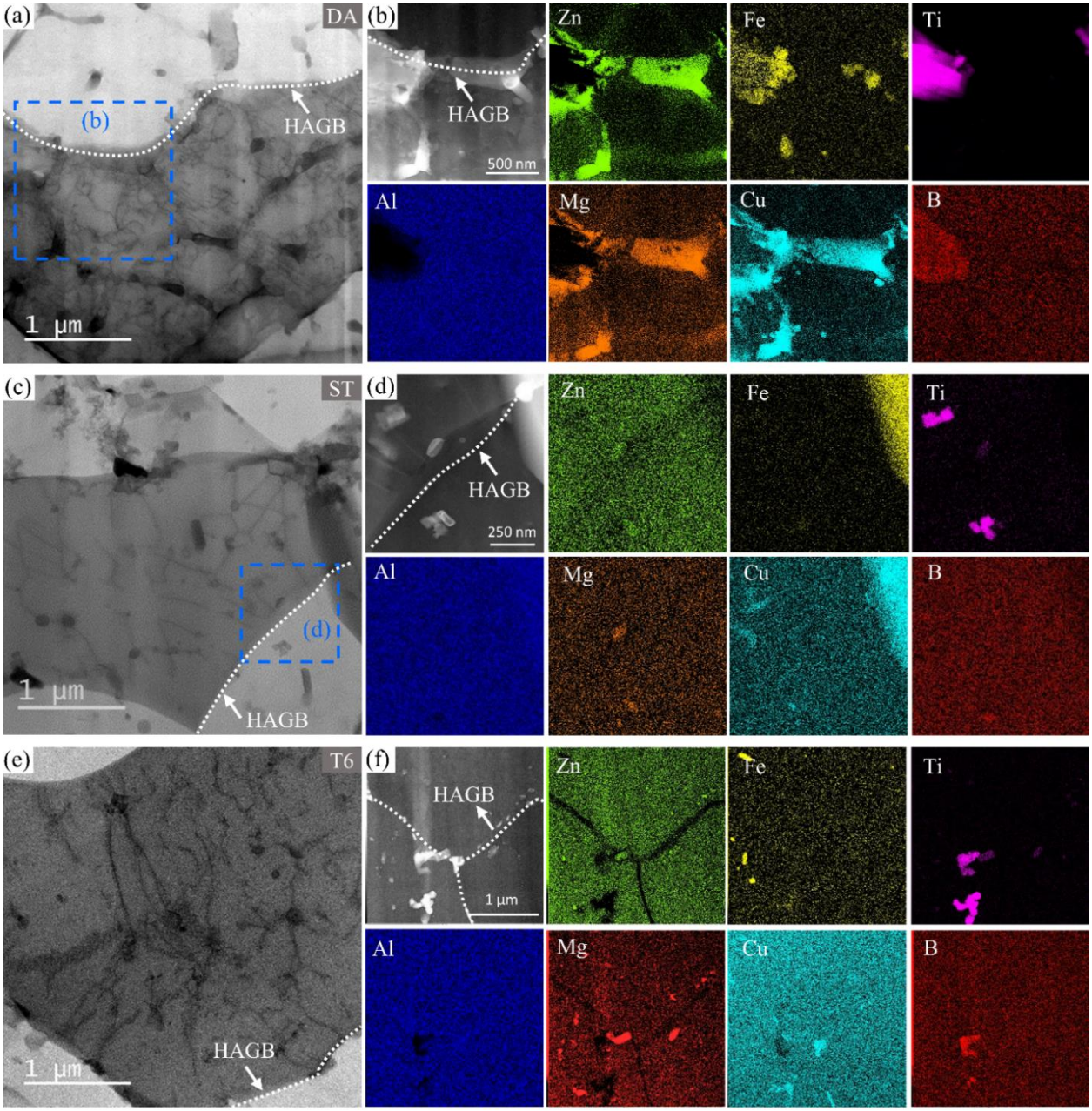

Fig. 8. ABF-STEM images of TiB_2/Al-Zn-Mg-Cu composite under (a) DA, (c) ST, and (e) T6 condition revealing the presence of dislocations, secondary phases, and grains with different orientations. The high diffraction contrast in the images indicates a high misorientation between the neighboring grains, with the HAGBs indicated by the dashed lines. HAADF-STEM images of a selected area containing HAGBs and the corresponding elemental EDS maps under (b) DA, (d) ST, and (f) T6 condition.

FOR THE PUBLISHED MANUSCRIPT, PLEASE VISIT ***ADDITIVE MANUFACTURING***: HTTPS://DOI.ORG/10.1016/J.ADDMA.2023.103460

3.2.3. *Nano-scale structure of the heat-treated samples*

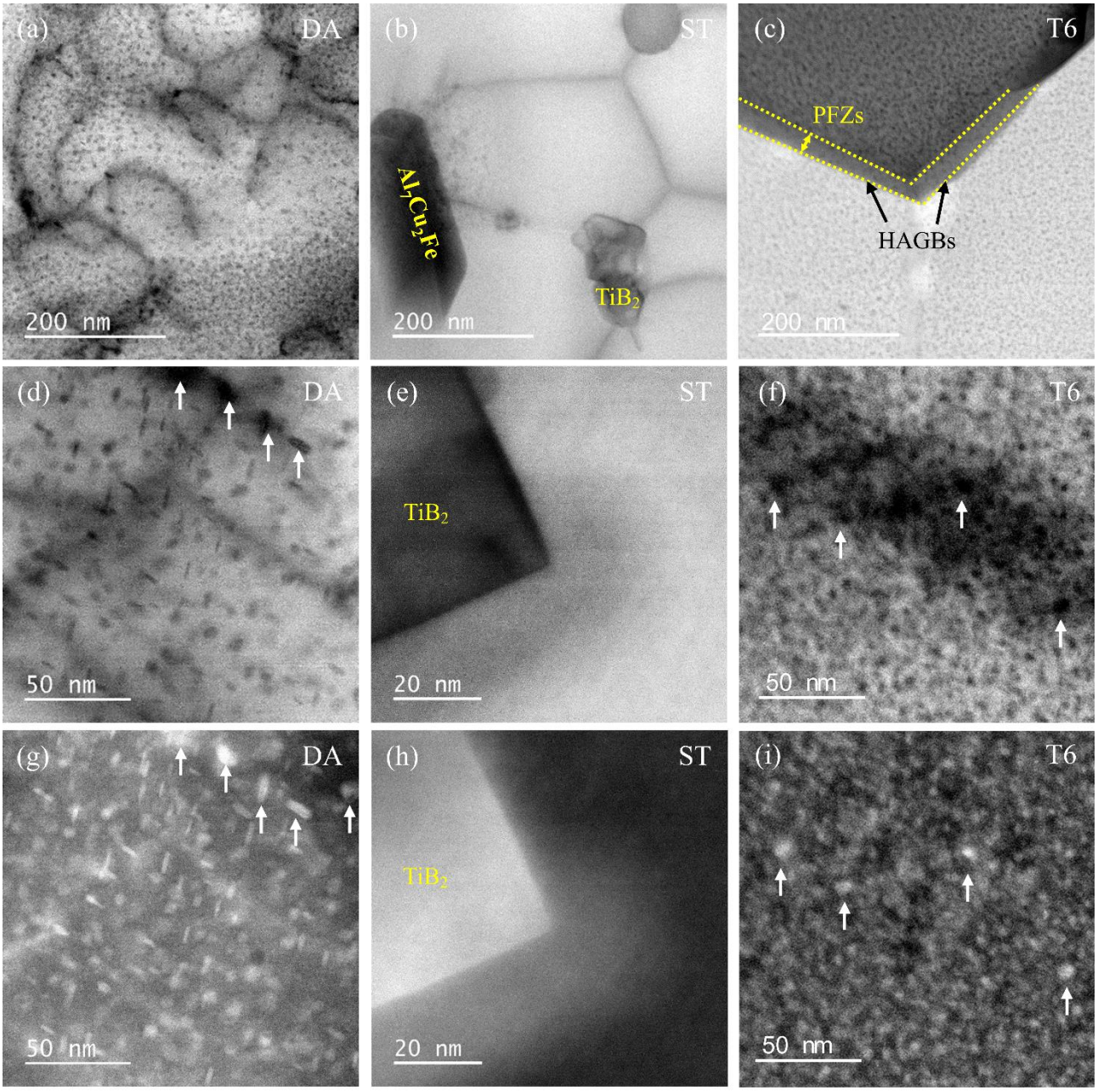

Fig. 9. ABF-STEM images of the TiB_2/Al-Zn-Mg-Cu matrix under (a) DA, (b) ST, and (c) T6 condition. (d-f) Higher magnification ABF-STEM and (g-i) corresponding HAADF-STEM images under DA, ST, and T6 conditions showing the morphology and distribution of precipitates under DA and T6 condition as well as the precipitate-free matrix under ST condition. Precipitate-free zones (PFZs) adjacent to the HAGBs in (c) are highlighted by the yellow dashed lines. The white arrows in (d, f, g, and i) point to the large precipitates adjacent to the dislocations.

At the nano-scale, the morphology and distribution of nanometer-sized precipitates in the Al matrix are studied using TEM. Fig. 9 shows the ABF- and HAADF-STEM images of heat-treated TiB_2/Al-Zn-Mg-Cu samples at higher magnifications, observed with a beam parallel to the [110] Al direction. A non-uniform distribution of precipitates can be observed in the DA sample (Figs. 9a, d, and g) due to the non-uniform distribution of dislocations and heterogeneous chemistry, as revealed by the EDS maps in Fig. 8b. A local high solute content induces a local high precipitate number density within the FCC-Al matrix. Moreover, as indicated by the white arrows in Figs. 9d and g, large precipitates, with

FOR THE PUBLISHED MANUSCRIPT, PLEASE VISIT ***ADDITIVE MANUFACTURING***: HTTPS://DOI.ORG/10.1016/J.ADDMA.2023.103460

a width of 5-6 nm and a length of around 13 nm for the platelets and a diameter of about 11 nm for the plate-like ones, are observed on the dislocation lines in the DA sample. A similar feature is also observed for the T6 sample with large plate-like precipitates shown 8-10 nm in diameter (Figs. 9f and i). It suggests that the dislocations are the favorable nucleation sites for the precipitates. Figs. 9b, e and h show that a precipitate-free Al matrix is obtained in the ST sample, except for the presence of TiB_2 particles and needle-shaped phases, which later are determined to be Al_7Cu_2Fe (Fig. 13). The T6 sample, on the other hand, contains a large amount of homogeneously distributed precipitates in the Al matrix (Figs. 9c, f, and i). Compared to the DA sample, the precipitate size is finer, and the number density is significantly higher in the T6 sample. Besides, precipitate-free zones (PFZs) with a width of around 30 nm are observed in the vicinity of HAGBs, which explains the Zn and Mg depletion observed in Fig. 8f. It is noteworthy that the PFZs in the TiB_2/Al-Zn-Mg-Cu composite do not show evidence of discontinuous/continuous grain boundary precipitates, which are commonly observed in the unreinforced Al-Zn-Mg-(Cu) alloys [10,41,42].

Fig. 10 presents the HRTEM image and the corresponding selected area FFT patterns for the TiB_2/Al-Zn-Mg-Cu alloy matrix under DA condition with beam parallel to the [101] Al zone axis. According to the morphological and crystallographic features, the precipitates in the Al matrix are confirmed to be the metastable η' precipitates. As the elemental distribution observed in Fig. 8 indicates that these precipitates are rich in Zn, Mg, and Cu, it can be concluded that they are η'-$Mg(Zn, Al, Cu)_2$ phase. The η' precipitates exhibit either a platelet (c and e in Fig. 10a) or a plate-like morphology (d in Fig. 10a). The FFT patterns confirm the growth of platelet η' on the (111) Al habit planes, with two variants of η' shown in Figs. 10 c and e, respectively, and one plate-like η' variant shown in Fig. 10d. These observations agree well with the previous findings on conventionally processed Al-Zn-Mg alloys [30,43]. The platelet η' precipitates have a thickness of 2-4 nm and a length of about 10 nm, and the plate-like ones show a diameter of about 6 nm. In addition, the FFT patterns in Figs. 10c and e show strong streaks along the (111) Al planes, as highlighted by the yellow arrows, which are associated with the presence of platelet η' precipitates. The plate-like η' precipitates attribute to the spots at the 1/3 and 2/3 $\{20\bar{2}\}$ positions, as shown in Fig. 10d.

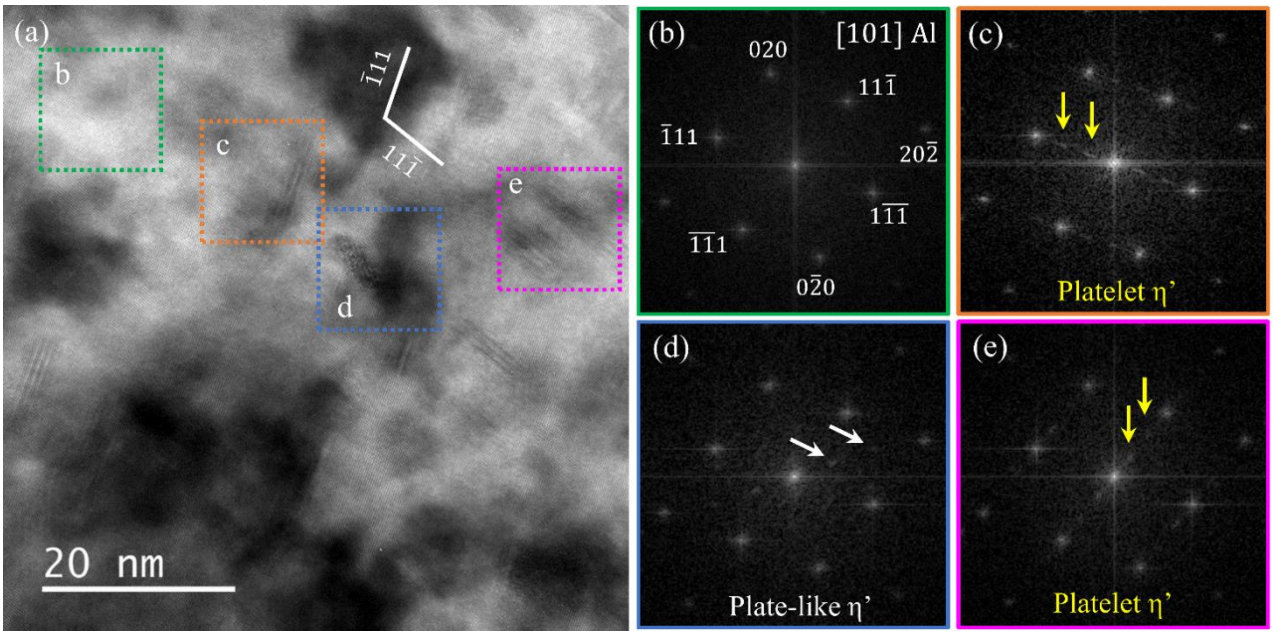

Fig. 10. (a) HRTEM image of the TiB_2/Al-Zn-Mg-Cu alloy under DA condition with beam parallel to [101] Al zone axis. (b) The corresponding FFT patterns of marked areas in (a) showing (b) the Al matrix, (c, e) platelet η' precipitates, and (d) plate-like η' precipitate. The arrows point to the diffraction spots of η' precipitates.

FOR THE PUBLISHED MANUSCRIPT, PLEASE VISIT ***ADDITIVE MANUFACTURING***: HTTPS://DOI.ORG/10.1016/J.ADDMA.2023.103460

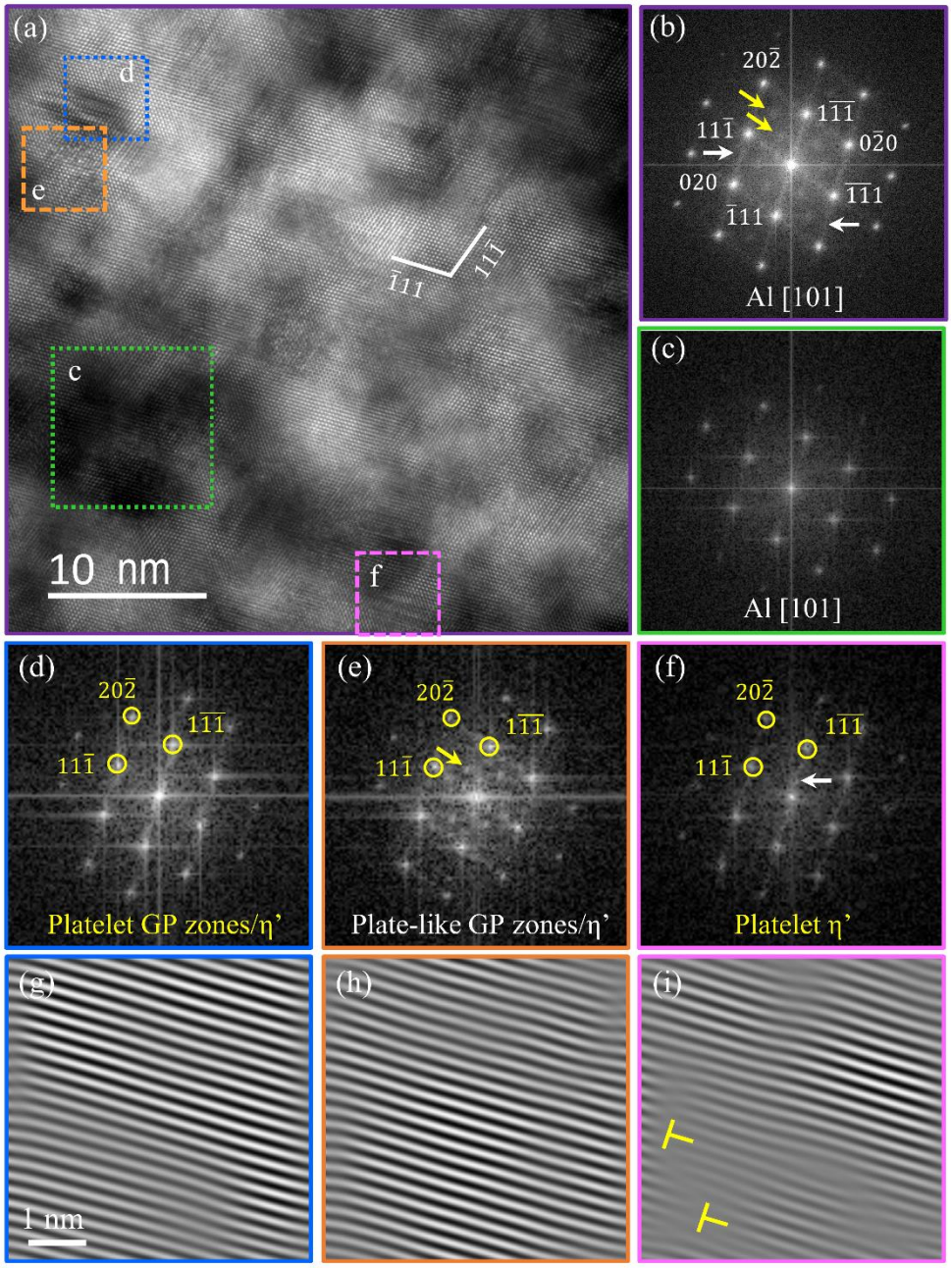

Fig. 11. (a) HRTEM image of the TiB_2/Al-Zn-Mg-Cu alloy under T6 condition, visualized along the [101] Al zone axis. (b) The corresponding FFT pattern of (a) with the yellow arrows pointing to the spots of the plate-like η' phase and horizontal white arrows pointing to the platelet η', forming streaks along the {111} Al planes. (c) The FFT patterns of an Al matrix collected from area c in (a). The FFT patterns and corresponding $(\bar{1}11)$ filtered inverse FFT patterns of (d, g) platelet GP zones/early stage η', (e, h) plate-like GP zones/early stage η', and (f, i) platelet η'.

To facilitate the comparison between the DA and T6 samples, HRTEM image and the corresponding selected area FFT patterns of T6-treated TiB_2/Al-Zn-Mg-Cu alloy are also imaged along the [101] Al zone axis and are shown in Fig. 11. Similar to the DA sample, the presence of platelet (d and f in Fig. 11a) on the {111} Al habit planes and plate-like (e in Fig. 11a) precipitates is observed in the T6 sample. The precipitate size in the T6 sample is evidently finer than that of the DA sample, showing an approximate thickness of 2-3 nm and a length of 6 nm for the platelet precipitates, and a diameter of 4-5 nm for the plate-like ones. Fig. 11b presents the corresponding FFT pattern of Fig.11a, revealing the reflections of the Al matrix, the diffraction spots at 1/3 $(20\bar{2})$ and 2/3 $(20\bar{2})$ positions attributed to

FOR THE PUBLISHED MANUSCRIPT, PLEASE VISIT ***ADDITIVE MANUFACTURING***: HTTPS://DOI.ORG/10.1016/J.ADDMA.2023.103460

the metastable plate-like η' phases, as indicated by the yellow arrows, as well as the streaks along the (111) Al planes associated with the platelet η' precipitates, as indicated by the horizontal white arrows. In addition, Figs. 11d-i show the individual diffraction pattern and the corresponding $(1\bar{1}\bar{1})$ filtered inverse FFT pattern of three selected precipitates (d, e, and f in Fig. 11a). Figs. 11 d, e, g, and h show that the platelet precipitate (d in Fig. 11a) and the plate-like precipitate (e in Fig. 11a are fully coherent with the Al matrix, indicating these are possibly early stage η' precipitates or GP zones. The GPII zones and early stage η' precipitates are generally reported not being distinguishable [44]. Figs. 11f and i indicate that the platelet precipitate (f in Fig. 11a) is a metastable η' precipitate and the presence of dislocations in its vicinity suggest that the η' precipitates are semi-coherent with the Al matrix.

3.3. Heterogeneous precipitation in the TiB_2/Al-Zn-Mg-Cu composite

3.3.1. Thermal analysis by DSC

To investigate the precipitation behavior of the L-PBF processed alloys, DSC thermal analysis was performed for the Al-Zn-Mg-Cu and TiB_2/Al-Zn-Mg-Cu alloys under both AB and ST conditions. Fig. 12 depicts the DSC heating curves of the samples at a scanning rate of 10 °C/min. The samples show three predominant peaks, namely, two exothermic peaks and one endothermic peak. The first exothermic peak at the 40 – 130 °C temperature range is associated with the formation of GP zones and followed by their dissolution, indicated by an endothermic peak at 130-150°C. Subsequently, the second exothermic peak is attributed to precipitation of η' and η. The formation and dissolution of GP zones and the precipitation of η'/η have also been reported in other Al-Zn-Mg(-Cu) based alloys [45,46]. The precipitation behavior in the TiB_2/Al-Zn-Mg-Cu composite occurs at lower temperatures (~ 230 °C in the as-built sample) compared to ~ 245 °C in the as-built Al-Zn-Mg-Cu alloy, indicating an accelerated precipitation in the composite. An earlier precipitation behavior can also be observed for the ST sample (~ 210 °C) as compared to the AB sample (~ 230 °C).

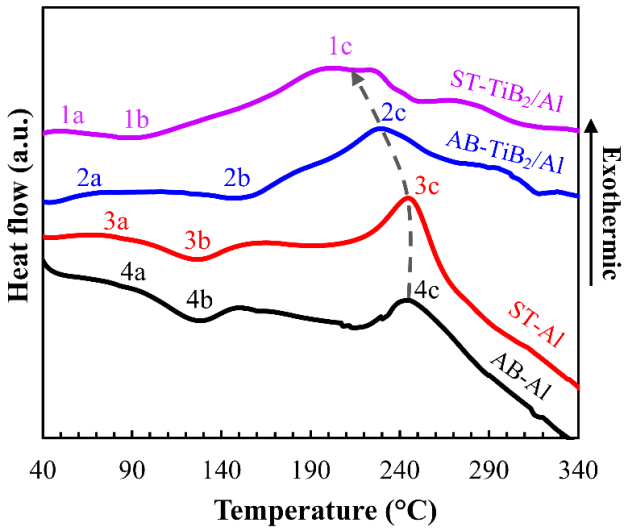

Fig. 12. DSC heating curves of Al-Zn-Mg-Cu and TiB_2/Al-Zn-Mg-Cu alloys under AB and ST conditions using a scanning rate of 10 °C/min.

3.3.2. Precipitation in the vicinity of the intermetallic phase

The crystallography and chemistry of the needle-shaped intermetallic phases, which are earlier observed in ST and T6 condition in Figs. 7k and l, are studied using TEM. The HAADF-STEM images in Fig. 13a and b give an overview of the TiB_2/Al-Zn-Mg-Cu alloy under ST and T6, respectively. Hexagonal and granular-shaped TiB_2 particles are indicated using blue arrows and the needle-shaped intermetallic phases are indicated using yellow arrows. The interfacial structure (Fig. 13d) and

FOR THE PUBLISHED MANUSCRIPT, PLEASE VISIT ***ADDITIVE MANUFACTURING***: HTTPS://DOI.ORG/10.1016/J.ADDMA.2023.103460

chemistry (Fig. 13g) of the needle-shaped phase and the Al matrix are further studied, confirming that the needle-shaped intermetallic phases are Al_7Cu_2Fe. The dark contrast at the Al_7Cu_2Fe/Al interface in the BF-TEM images (Figs. 13a and c) could be attributed to the existence of dislocations, suggesting a large lattice mismatch between Al_7Cu_2Fe and Al. The associated SAED patterns shown in Figs. 13c and d confirm the existing OR between Al_7Cu_2Fe and Al, namely, [210]Al_7Cu_2Fe//[101]Al, (001)Al_7Cu_2Fe // (020)Al. The HAADF-STEM image in Fig. 13e show the formation of precipitates on the Al_7Cu_2Fe and TiB_2 particles in the T6 alloy. A closer look at the Al_7Cu_2Fe/Al interface (Fig. 13f) and the corresponding elemental EDS maps (Fig. 13g) reveal the presence of PFZs with a width of about 15 nm at the Al_7Cu_2Fe/Al interface. The presence of PFZs is also observed at the HAGBs (width of around 30 nm), as previously shown in Fig. 8. This observation suggests that PFZs are prone to form at the incoherent interfaces and HAGBs that are typically labeled as high energy boundaries [10,30]. The presence of needle-shaped intermetallic Al_7Cu_2Fe phases has been reported to embrittle the material and promote corrosion pitting [47], thus the Fe impurity amount should be strictly limited in the future alloy development.

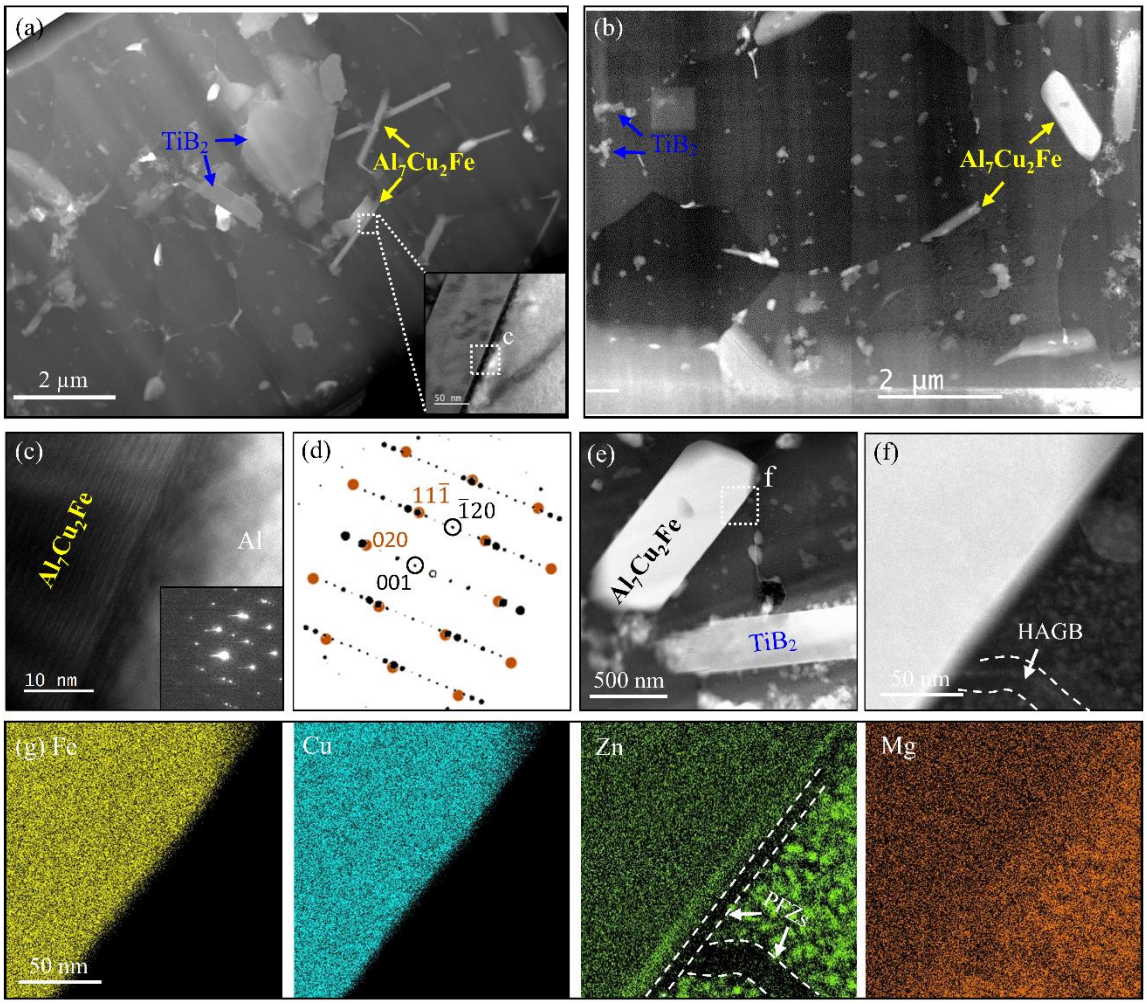

Fig. 13. HAADF-STEM images of the TiB_2/Al-Zn-Mg-Cu alloy under (a) ST and (b) T6 conditions. The inserted BF-TEM image in (a) showing the Al_7Cu_2Fe phase and the surrounding Al matrix. (c) BF-STEM image of the selected area in (a). The lattice fringe in Al_7Cu_2Fe is visible at higher magnification. The insert shows the associated SAED pattern of area in (c). (d) The indexed SAED pattern showing an OR: [210]Al_7Cu_2Fe // [101]Al, (001) Al_7Cu_2Fe // (020)Al. (e) HAADF-STEM image of the T6 TiB_2/Al-Zn-Mg-Cu sample showing the formation of precipitates on the Al_7Cu_2Fe and TiB_2 particles. (f) HAADF-STEM image of the selected area in (e) showing the Al_7Cu_2Fe/Al interface. (g) The corresponding elemental EDS maps of (f) showing the PFZs at the Al_7Cu_2Fe/Al interface.

FOR THE PUBLISHED MANUSCRIPT, PLEASE VISIT ***ADDITIVE MANUFACTURING***: HTTPS://DOI.ORG/10.1016/J.ADDMA.2023.103460

3.3.3. Precipitation on the TiB_2 particles and in their vicinities

Fig. 14 shows the presence of large precipitates containing Zn, Mg, and slight Cu on the TiB_2 particles as well as on the LAGBs in the TiB_2/Al-Zn-Mg-Cu sample after ageing, suggesting that the TiB_2/Al interfaces and the LAGBs are preferential nucleation sites for the η'/η precipitates. The formation of precipitates on the Al_7Cu_2Fe phase is also observed as previously shown in Fig. 13. These precipitates show an average chemistry of $(Zn_{2.0}Cu_{1.4})Mg$ (at%) determined by STEM-EDS. In addition, a continuous Zn, Mg, and Cu-rich layer with a thickness of 1-2 nm is identified at the TiB_2/Al interface (Fig. 14b), suggesting the segregation of solutes at the TiB_2/Al interface. The BF-TEM image in Fig. 14c reveals a higher dislocation density in the Al matrix adjacent to the TiB_2 particle than in the Al matrix away from the particles in the DA sample. However, such an increased dislocation density is not evident in the water-quenched ST sample (Fig. 9). The increased dislocation density in the DA sample is mainly resulting from the thermal expansion coefficient mismatch between Al (24×10^{-6} K^{-1}) and TiB_2 (7.8×10^{-6} K^{-1}) during the L-PBF solidification process [48]. The steep temperature gradient (10^6 - 10^7 K/m) and the cyclic heating and cooling effect during the L-PBF process [14,49] promote dislocation generation. Meanwhile, the HAADF-STEM image in Fig. 14d shows the presence of relatively large precipitates with an approximate width of 6 nm and length of 15 nm, located on the dislocations in the vicinity of the TiB_2 particles, confirming a locally accelerated precipitation behavior. It is worth noting that the distribution of η' precipitates is right next to the TiB_2/Al interface, as indicated by the arrows in Figs. 14d and e. This feature is different from that observed at the incoherent Al_7Cu_2Fe/Al interface (Fig. 13) and HAGBs (Fig. 9c) in the present work, as well as the incoherent B_4C/Al interface reported by Wu et al. [30], where noticeable PFZs are present. The presence of PFZs at the incoherent interface or GBs with large misorientations is mainly due to the extensive vacancy annihilation in the neighboring matrix and mass transport of solutes along the high energy boundaries [10]. The presence of PFZs and the presence of coarse precipitates in the center of PFZs are detrimental to the static tensile and dynamic fatigue properties, as well as the stress corrosion cracking resistance due to the increased localized stress concentration and electrochemical contrast [10,50]. Hence, the semi-coherent TiB_2/Al interfaces that characterized by an excellent interfacial bonding [21] can strengthen the material, promote the precipitation behavior, and avoid the formation of PFZs at the TiB_2/Al interfaces under the peak age condition, providing great potential benefits for the mechanical performance.

FOR THE PUBLISHED MANUSCRIPT, PLEASE VISIT ***ADDITIVE MANUFACTURING***: HTTPS://DOI.ORG/10.1016/J.ADDMA.2023.103460

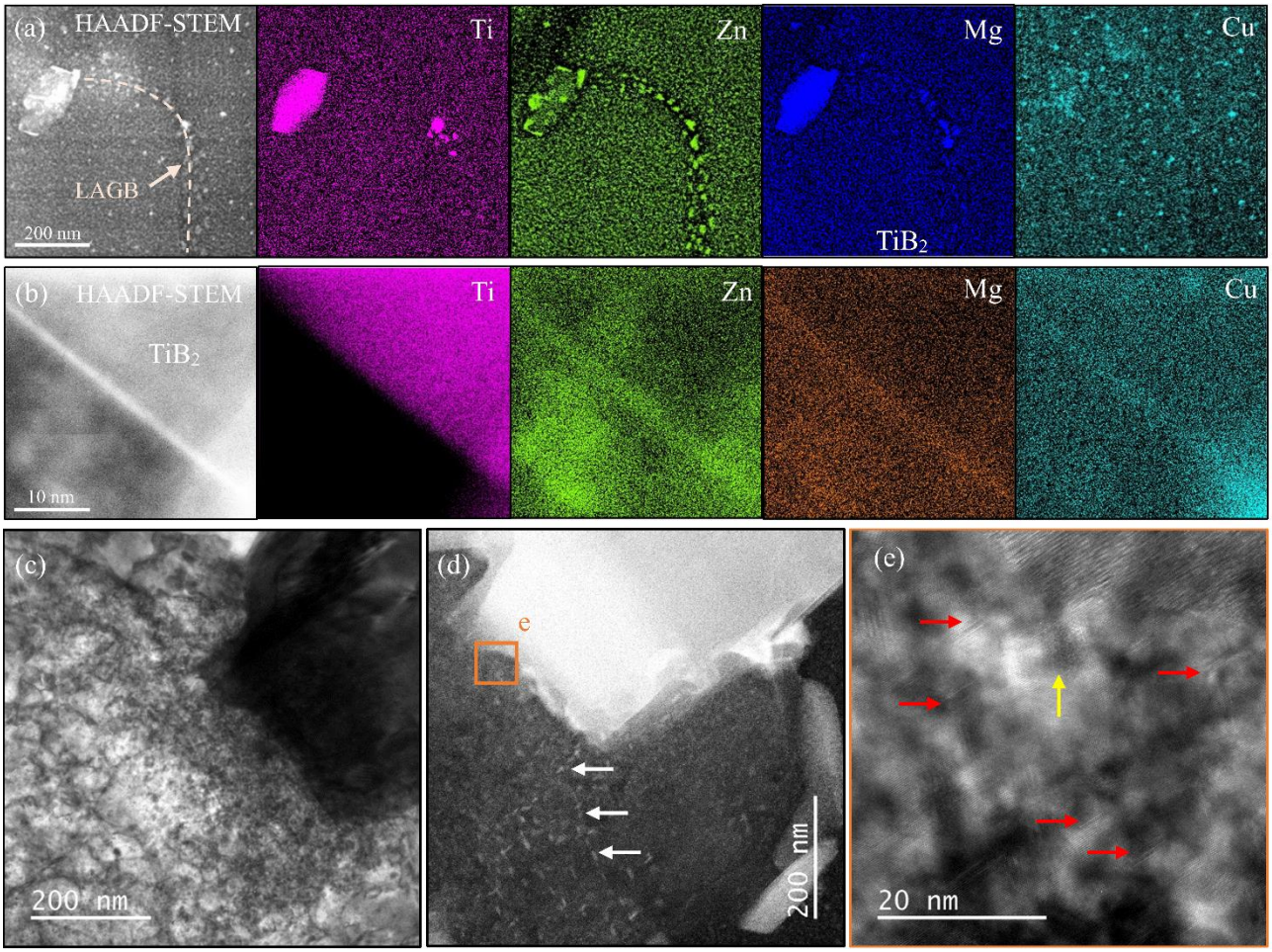

Fig. 14. HAADF-STEM image and the associated elemental EDS maps of the TiB_2/Al-Zn-Mg-Cu sample under T6 condition showing (a) the large precipitates on the TiB_2 particles and low-angle grain boundary. (b) the continuous segregation layer (1-2 nm) at the TiB_2/Al interface. (c) BF-TEM image of the TiB_2/Al-Zn-Mg-Cu sample under DA condition showing the increased dislocation density in the Al matrix adjacent to the micron-sized TiB_2 particle located at the grain boundary. (d) HAADF-STEM image of the TiB_2/Al-Zn-Mg-Cu sample under DA condition showing the presence of large precipitates adjacent to the TiB_2 particle due to the presence of dislocations. (e) The associated HRTEM image of region e in (d) showing the distribution of precipitates in the vicinity of submicrometer-sized TiB_2 particle. The platelets are indicated by the horizontal red arrows, and the plate-like one is indicated by the vertical yellow arrow.

3.3.4. Precipitation at HAGBs

Fig. 15 presents the microstructural features at the HAGBs in the T6 TiB_2/Al-Zn-Mg-Cu composite. As reported previously in Figs. 8f and 9c, the presence of PFZs with a width of around 30 nm at the HAGBs is observed. However, the presence of large Zn and Mg(Cu)- rich precipitates at the HAGBs, which is commonly reported in the Al-Zn-Mg-Cu alloy [10,41,42,50], is not evident in the TiB_2/Al-Zn-Mg-Cu composite. Nevertheless, a few large Cu-rich precipitates (~130 nm) are observed, which are deduced to be Al_2Cu (Figs. 15a and c). The deficiency of Zn, Mg, and Cu-rich precipitates at the HAGBs might be related to the preferential precipitation of η'/η precipitates on the grain boundary TiB_2 particles, as observed in Fig. 15b. Near the large Cu-rich precipitates, the segregation of Zn, Mg, and Cu at the HAGBs observed in Fig. 15c provides an indication for the diffusion of alloying elements along the HAGBs.

FOR THE PUBLISHED MANUSCRIPT, PLEASE VISIT ***ADDITIVE MANUFACTURING***: HTTPS://DOI.ORG/10.1016/J.ADDMA.2023.103460

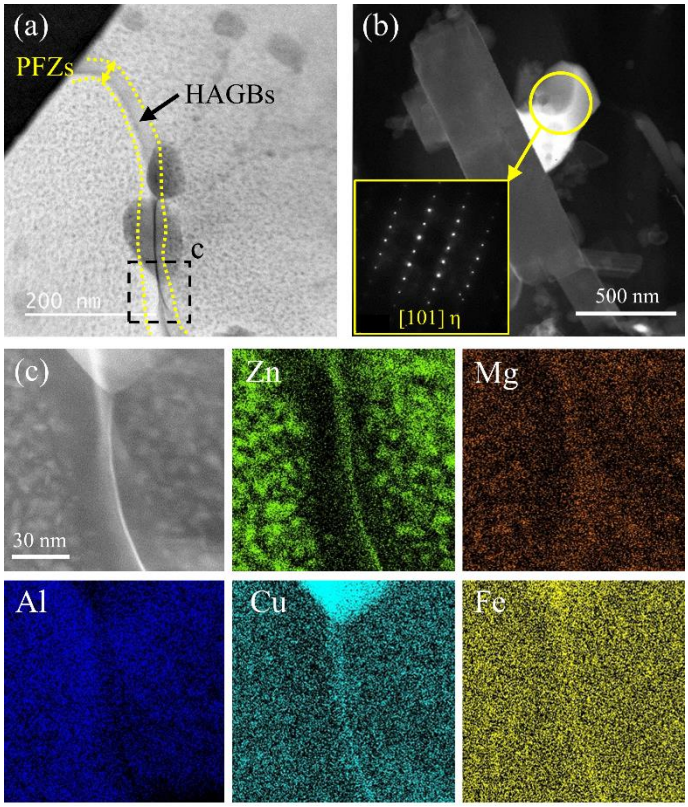

Fig. 15. (a) ABF-STEM image of the TiB_2/Al-Zn-Mg-Cu sample under T6 condition showing the PFZs and grain boundary precipitates. (b) HAADF image showing the big precipitate grown on the TiB_2 particles at the grain boundary, with the inserted SAED pattern confirming the presence of stable η precipitates. (c) The corresponding EDS maps of area c in (a) showing the segregation of alloying elements at the HAGBs.

4. Discussion

4.1. Grain refinement mechanism and mitigation of hot cracking

The present work demonstrated that the strong-textured columnar grains in the LPBF-processed Al-Zn-Mg-Cu alloy were modified into an isotropic equiaxed grain structure in the TiB_2/Al-Zn-Mg-Cu composite, accompanied by a significant grain size reduction from 53.3 ± 28.2 to 2.0 ± 0.9 μm (Fig. 3). Consequently, severe hot cracking during LPBF of the Al-Zn-Mg-Cu alloy, was effectively eliminated in the TiB_2/Al-Zn-Mg-Cu composite. The fine equiaxed grains mainly owe their high crack resistance to the high strain accommodation ability by grain rotation in the vulnerable zone [20,51], disrupted thermal stress build-up provided by the numerous neighboring grain boundaries [52], and suppressed crack propagation due to the presence of tortuous grain boundaries [51,53]. The hot cracking mechanisms have been reported by other researchers [38,54–57]. This section will mainly focus on the grain refinement mechanisms in the TiB_2/Al-Zn-Mg-Cu composite.

According to the interdependence model, the final grain size of a material greatly depends on the solutes-attributed constitutional undercooling ΔT_{CS} and the process-associated thermal undercooling ΔT_{therm}, which govern the nucleation events during solidification, as well as the critical nucleation undercooling ΔT_n, which is the nucleation energy barrier that could be dramatically reduced by introducing potential nucleants [22,58,59]. Characteristics such as a large temperature gradient (10^6 K/m) and directional heat dissipation, which are intrinsic to the L-PBF process, as well as the presence of a positive temperature gradient at the solid/liquid interface, provoke the epitaxial growth of columnar grains in the Al-Zn-Mg-Cu alloy [37,60]. For a particular L-PBF process condition, i.e. using

FOR THE PUBLISHED MANUSCRIPT, PLEASE VISIT ***ADDITIVE MANUFACTURING***: HTTPS://DOI.ORG/10.1016/J.ADDMA.2023.103460

an identical LPBF process parameter set, the variations in ΔT_{therm} of the two studied Al-Zn-Mg-Cu alloys with and without TiB_2 can be neglected. Thus, the grain refinement effect in the TiB_2/Al-Zn-Mg-Cu alloy is predominantly attributed to the reduced ΔT_n as heterogeneous nucleation is promoted by the TiB_2 inoculant particles, and increased ΔT_{CS} due to the excessive solute content compared to the reference Al-Zn-Mg-Cu alloy.

Over the past few decades, the grain refinement mechanisms in the Al-Ti-B system have been a topic of debate. Whether the Al grains directly nucleate on the TiB_2 phase or on an Al_3Ti monolayer that is formed in-situ on the basal planes of TiB_2 [61–63]. Other researchers [64] have reported that the presence of an excessive amount of Ti solutes could ensure a significantly higher grain refinement efficiency. In the present work, both the feedstock powder and the as-built sample show a Ti:B atomic ratio of 1:2 according to the chemical composition measured by ICP-OES (Table 1). Besides, no trace of Al_3Ti layer was identified at the Al/TiB_2 interface by TEM. Thus, it suggests that the heterogeneous nucleation event of Al grains was triggered by the TiB_2 particles.

According to Turnbull and Vonnegut's theory [65], the ΔT_n is exponentially proportional to the lattice mismatch δ between the FCC-Al and the nucleants, which is given by,

$$\Delta T_n = \frac{c_\epsilon}{\Delta S_V}\delta^2 \quad (1)$$

where c_ϵ and ΔS_V (J/K/m^3) denote the elastic coefficient and entropy of fusion, respectively. Thus, a small δ, namely, a good crystallographic coherency, between the nucleants and FCC-Al, promotes the grain refinement effect [66]. The lattice mismatch including the interatomic mismatch δ_a and interplanar mismatch δ_p can be assessed by the edge-to-edge matching (E2EM) model [29]. Considering a lattice parameter of a = 0.40494 nm for FCC-Al and lattice parameters of a = 0.3009 nm and c = 0.3262 nm for HCP-TiB_2 [67], the lattice mismatch between TiB_2 and FCC-Al for the following ORs are assessed,

The OR-A: $[2\bar{1}\bar{1}0]_{TiB2}//[101]_{Al}$, δ_a= -6.1%, $(01\bar{1}1)_{TiB2}//(020)_{Al}$, δ_p= -0.9%

The OR-B: $[1\bar{1}00]_{TiB2}//[\bar{1}\bar{1}2]_{Al}$, δ_a= -6.1%, $(11\bar{2}0)_{TiB2}//(\bar{2}20)_{Al}$, δ_p= -6.1%

The OR-C: $[2\bar{1}\bar{1}0]_{TiB2}//[101]_{Al}$, δ_a= -6.1%, $(0\bar{1}10)_{TiB2}//(\bar{1}\bar{1}1)_{Al}$, δ_p= -12.5 %

The OR-A with the minimum lattice mismatch has been observed by TEM (Fig. 5), confirming the heterogeneous nucleation behavior of Al grains on the TiB_2 particles. The small lattice mismatch between the TiB_2 inoculants and the Al matrix provided low-energy interfaces during heterogeneous nucleation, which reduced the critical nucleation undercooling energy barrier and promoted effective grain refinement [29].

Additionally, the excessive solute content, namely, Zn, Mg, and Cu, in the TiB_2/Al-Zn-Mg-Cu alloy, compared to the virgin Al-Zn-Mg-Cu alloy, could also contribute to a grain refinement effect by generating constitutional undercooling ahead of the solid/liquid interface [68]. The effect of solutes can be evaluated by the growth restriction factor Q. For a multi-component alloy system, the Q can be defined as,

$$Q = \sum m_i(k_i - 1)C_i \quad (2)$$

where m_i, k_i, and C_i are the equilibrium liquidus slope, partition coefficient, and solute concentration, respectively, of binary alloys for individual element [9]. This model assumes no interactions between the solutes. According to the chemical composition given in Table 1, the studied Al-Zn-Mg-Cu and TiB_2/Al-Zn-Mg-Cu alloy show a Q-value of 11.6 and 14.9 K, respectively, showing a slightly higher grain growth restriction effect in the latter due to the higher solute content. It should be noted, however,

FOR THE PUBLISHED MANUSCRIPT, PLEASE VISIT ***ADDITIVE MANUFACTURING***: HTTPS://DOI.ORG/10.1016/J.ADDMA.2023.103460

that the liquidus slope and partition coefficient under rapid solidification conditions, representative for processes such as L-PBF, might deviate from the equilibrium values, resulting in less constitutional undercooling [69].

4.2. Accelerated precipitation kinetics

According to the DSC results presented in Fig. 6, the TiB_2/Al-Zn-Mg-Cu composite showed an accelerated precipitation of η'/η compared to the virgin Al-Zn-Mg-Cu alloy. The main factors that are responsible for the accelerated precipitation behavior in the TiB_2/Al-Zn-Mg-Cu composite are summarized below.

4.2.1. Heterogeneous precipitation on the crystallographic defects

As reported earlier, large precipitates containing Zn, Mg, and Cu are observed on different crystallographic defects, including the dislocations in the grain interior resulting from solidification (Fig. 9), semi-coherent TiB_2/Al interfaces (Figs. 13-15), dislocations in the vicinity of the TiB_2 particles due to thermal mismatch (Fig. 15), in-coherent Al_7Cu_2Fe/Al interfaces (Fig. 13), and LAGBs (Fig. 14) in the TiB_2/Al-Zn-Mg-Cu sample after ageing. It suggested that these crystallographic defects are the preferential nucleation sites for the η'/η precipitates. The accelerated precipitation on these crystallographic defects can be attributed to the reduced nucleation energy barrier for heterogeneous nucleation compared to that required for homogeneous nucleation in the bulk material [10,50]. The presence of TiB_2 particles in the composite introduced a large number of TiB_2/Al interfaces as well as thermal mismatch dislocations in the vicinity of the particles, promoting heterogeneous precipitation, and hence, accelerated precipitation.

4.2.2. Enhanced diffusion along the HAGBs

The second factor contributing to the accelerated precipitation kinetics in the TiB_2/Al-Zn-Mg-Cu composite is the larger amount of HAGBs. Fig. 3 showed that the TiB_2/Al-Zn-Mg-Cu composite contains significantly refined grains (2.0 ± 0.9 μm) and a higher fraction of HAGBs (69.7%), hence, a substantially higher amount of HAGBs, compared to the Al-Zn-Mg-Cu alloy with an average grain size of 53.3 ± 28.2 μm and a HAGBs fraction of 64.5%. Notwithstanding the fact that elemental segregation at HAGBs was not distinguishable by EDS-STEM in the ST sample probably due to the detection limit (Fig. 8d). The segregation of Zn, Mg, and Cu to the HAGBs after ST has been confirmed by Sha et al. [70] and Zhao et al. [10] using atom probe tomography in severely deformed and as-quenched Al-Zn-Mg-Cu alloys, respectively. The local higher solute concentration at the grain boundary, resulting from equilibrium grain boundary segregation driven by Gibbs adsorption isotherm, facilitates an earlier precipitation behavior at the HAGBs [71]. Due to the local solute partitioning between the HAGBs and the adjacent matrix, and potential depletion of vacancies near the HAGBs, PFZs with 5-100 nm width are generally observed near the HAGBs depending on the duration of the ageing heat treatment [41,42,50]. As shown in Fig. 8f and Fig. 9c, the presence of PFZs with a width of around 30 nm is observed at the HAGBs in the TiB_2/Al-Zn-Mg-Cu composite when T6 heat treated. In addition, during the precipitation process, the HAGBs act as fast diffusion channels transporting solute elements, hence, accelerating precipitation [10]. The segregation of Zn, Mg, and Cu at the HAGBs, observed in Fig. 15c, provides an indication for the diffusion of alloying elements along the HAGBs. It should be mentioned that the elimination of hot cracks can also enhance the diffusion kinetics in the TiB_2/Al-Zn-Mg-Cu composite.

FOR THE PUBLISHED MANUSCRIPT, PLEASE VISIT ***ADDITIVE MANUFACTURING***: HTTPS://DOI.ORG/10.1016/J.ADDMA.2023.103460

4.2.3. Increased chemical driving force for precipitation

The locally higher solute concentration and higher supersaturation level in the matrix provides a higher chemical driving force for precipitation, thus accelerating the precipitation kinetics [72].

In the present work, as shown in Fig. 14b, the segregation of solutes (Zn and Mg) was identified at the TiB_2/Al interface, resulting in a locally higher Zn and Mg solute concentration than in the Al matrix. Similar findings on preferential segregation of Mg at the B_4C/Al interface [73], Zn at the SiC/Mg interface [74], and Cu at the Al_3BC/Al and MgB_2/Al interface [31] have been reported. In addition, as listed in Table 1, excessive Zn and Mg were added to the TiB_2/Al-Zn-Mg-Cu feedstock powder to compensate for their evaporation losses during the L-PBF process, resulting in a higher Zn and Mg content in the as-built and as-quenched samples. Considering an ideal solution behavior of a dilute binary alloy system, the chemical driving force ΔG_{ch} is proportional to the supersaturation level, X_0/X_e, where X_0 is the solute concentration in solid solution, X_e is the equilibrium solvus of solute in α-Al. The chemical driving force for precipitation [75] in such a binary system is given by:

$$\Delta G_{ch} = \frac{RT}{V_\eta}\left(\frac{X_\eta - X_e}{1 - X_e}\right)\ln\frac{X_0}{X_e} \quad (1)$$

where X_η is the molar fraction of solute in the η precipitate. A higher Zn and Mg content at the TiB_2/Al interface leads to locally accelerated precipitation at the interface. A higher Zn and Mg content in the TiB_2/Al-Zn-Mg-Cu composite, compared to the virgin Al-Zn-Mg-Cu alloy, enables a higher supersaturation level and leads to a higher chemical driving force as well as reduced activation energy barrier, facilitating precipitate formation. Thus, the heterogeneous precipitation effect, the enhanced diffusion along the HAGBs, along with the higher chemical driving force for precipitation facilitate a faster nucleation and growth of η'/η precipitations in the TiB_2/Al-Zn-Mg-Cu composite during the ageing process.

4.3. Microstructural features contributing to microhardness

The strength of the Al-Zn-Mg-Cu-based alloys with and without nanoparticles under different heat treatment conditions is the result of synergistic strengthening effects resulting from a combination of grain refinement, particle reinforcement, solid solution, precipitation, and dislocations. The microstructural features under different heat treatment conditions are compared and their associated strengthening mechanisms are discussed in this section.

4.3.1. Effect of nanoparticles

The hardness curves in Fig. 6 showed that the TiB_2/Al-Zn-Mg-Cu composite exhibited a superior hardness as compared to the reference Al-Zn-Mg-Cu alloy under all the heat treatment conditions. Take the as-built samples as an example, the TiB_2/Al-Zn-Mg-Cu composite obtained a significantly higher hardness of 163 ± 6 HV compared to the reference Al-Zn-Mg-Cu alloy (97 ± 7 HV). This hardness increment can be attributed to the following factors,

$$\Delta H = \Delta H_{GB} + \Delta H_{LB} + \Delta H_{OR} + \Delta H_{CET} \quad (2)$$

where ΔH_{GB}, ΔH_{LB}, ΔH_{OR}, and ΔH_{CET} indicate the hardness increase contribution by grain boundaries, load transfer, Orowan bypassing, and thermal mismatch strengthening, respectively.

The TiB_2/Al-Zn-Mg-Cu composite showed a significantly smaller grain size of 2.0 ± 0.9 μm compared to the reference Al-Zn-Mg-Cu alloy (53.5 ± 28.2 μm), which provides additional grain boundary strengthening. The grain boundary strengthening can be estimated by the Hall-Petch relationship [76],

$$\Delta H_{GB} = k_{H-P}d^{-0.5} - k_{H-P}d_0^{-0.5} \quad (3)$$

FOR THE PUBLISHED MANUSCRIPT, PLEASE VISIT ***ADDITIVE MANUFACTURING***: HTTPS://DOI.ORG/10.1016/J.ADDMA.2023.103460

where the constant k_{H-P} is 17.3 × 10^{-3} kg/$m^{3/2}$ for the aluminum alloy [76], d and d_0 are the grain size with and without grain refinement. The grain refinement effect in the composite contributed to a hardness increase of ~ 10 HV as compared to the Al-Zn-Mg-Cu alloy.

The TEM results in Fig. 4 revealed a coherent Al/TiB_2 interface. A strong interface bonding could strengthen the material by load-bearing mechanism [21], which can be calculated as follows,

$$\Delta H_{LB} = 0.15 V_p \sigma_i \quad (4)$$

where V_p is the volume fraction of the reinforcement particles, σ_i is the bonding strength of the Al/TiB_2 interface ~ 676 MPa [21]. Therefore, 3.43 vol% of TiB_2 particles could contribute to a hardness increment of ~ 3 HV.

The presence of TiB_2 nanoparticles in the Al grain matrix could hinder the motion of dislocations during deformation by looping around the nanoparticles. The hardness increment by Orowan strengthening can be given by the following equation [77],

$$\Delta H_{OR} = \frac{0.4MGb}{9.807\pi L} \frac{\ln\left(\frac{d_p \pi}{2b}\right)}{\sqrt{1-\upsilon}} \quad (5)$$

$$L = d_p \left(\sqrt{\frac{2\pi}{43}} - \frac{\pi}{2} \right) \quad (6)$$

where M, G, and b are the average Taylor factor (~ 3.06 for Al), shear modulus of the matrix (~ 26.9 GPa), and the Burgers vector (~ 0.286 nm), respectively. $\upsilon = 0.33$ is the Poisson's ratio of the Al matrix. d_p and L are the particle size and inter-particle spacing, respectively. Thus, 3.43 vol% of TiB_2 particles with a particle size of ~40 nm could contribute to an upper bound hardness increment of ~19 HV.

The difference in thermal expansion coefficient between the TiB_2 particles (7.8×10^{-6} K^{-1}) and the Al matrix (24×10^{-6} K^{-1}) resulted in the formation of dislocations in the vicinity of the TiB_2 particles during solidification, particularly for the L-PBF-processed composite, as observed in Fig. 13 [48,78]. The thermal mismatch strengthening effect can be estimated according to the following equation [48],

$$\Delta H_{CET} = \frac{\alpha}{9.807} Gb \sqrt{\frac{12\Delta T \Delta\alpha V_p}{(1-V_p)bd_p}} \quad (7)$$

where $\alpha = 1.25$ is a constant. ΔT = 485 K is the difference between solidus and room temperature. The solidus temperature (783 K) of the composite is calculated using a Thermo-Calc software and TCAL6: Al-Alloys V6.0 database. $\Delta\alpha$ is the thermal expansion coefficient mismatch between TiB_2 and Al (16.2×10^{-6} K^{-1}). Hence, 3.43 vol% of TiB_2 particles with a particle size of ~40 nm could contribute to an upper bound hardness increment of ~17 HV.

The above-mentioned strengthening mechanisms, attributed to the presence of TiB_2 particles, give a total hardness increment of ~49 HV, which is slightly lower than the experimental hardness increment of ~ 66 HV. It should be noted that the presence of an excessive alloying element content, including Zn, Mg, and Cu, in the composite compared to the unmodified Al-Zn-Mg-Cu alloy (Table 1) could also contribute to a higher hardness in the TiB_2/Al-Zn-Mg-Cu composite. Additionally, the presence of hot cracks in the unmodified Al-Zn-Mg-Cu alloy could deteriorate its hardness.

4.3.2. Effect of heat treatments

As shown in Fig. 6, the application of a heat treatment affects the hardness of a material significantly. The TiB_2/Al-Zn-Mg-Cu composite showed the following hardness trend when heat treated under different conditions: AB < ST < DA < T6. As the TiB_2 particles are thermodynamically stable in the

FOR THE PUBLISHED MANUSCRIPT, PLEASE VISIT ***ADDITIVE MANUFACTURING***: HTTPS://DOI.ORG/10.1016/J.ADDMA.2023.103460

aluminum matrix [21], the hardness alteration due to heat treatment variations can mainly attributed to the modification of the microstructure. Both the amount and distribution of precipitates and dislocations changes upon heat treatment. Based on the experimental results, the main microstructural features governing the mechanical performance of the TiB_2/Al-Zn-Mg-Cu composite under DA, ST, and T6 conditions are schematically illustrated in Fig. 15.

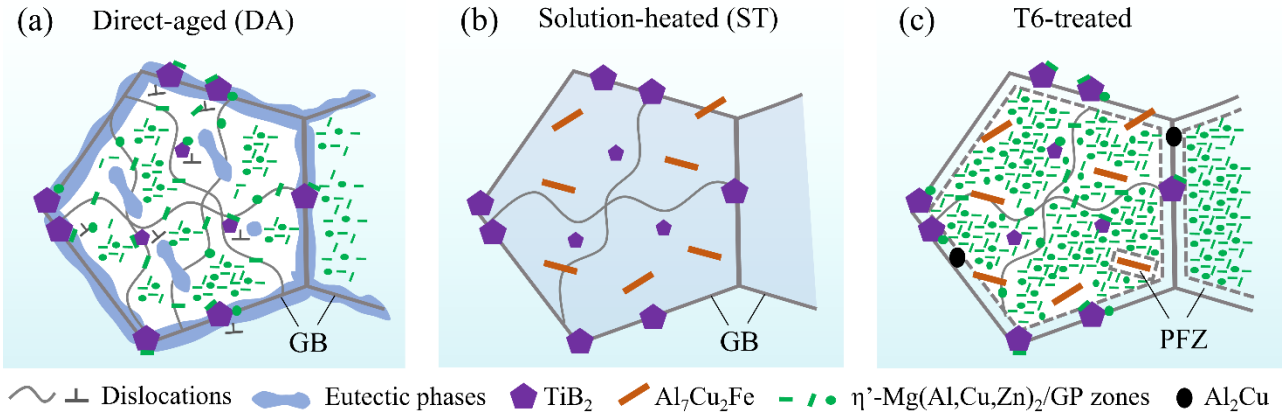

Fig. 16. Schematic diagram indicating the distribution of precipitates, eutectic phases, and dislocations in the Al matrix under (a) DA, (b) ST, and (c) T6 condition.

According to the TEM-EDS results, the chemical composition of the Al matrix and the grain boundary eutectic phases in the TiB_2/Al-Zn-Mg-Cu composite under DA, ST, and T6 conditions are presented in Table 2. It should be noted that the TEM-EDS results tend to overestimate the Cu content due to the Cu contamination from the grid. As observed in Figs. 4 and 8, profound microsegregation of Zn, Mg, Cu, and Fe was observed in the AB samples and was preserved in the DA samples, forming eutectic phases at the grain boundary. The alloying elements in the Al matrix stayed in solid solution in the AB condition and precipitated as η'/η precipitates in the DA condition. Meanwhile, the high dislocation density resulting from the L-PBF process was maintained after the DA heat treatment. The solution heat treatment enabled the dissolution of most of the segregated alloying elements and resulted in an even higher Al matrix supersaturation level, as shown in Table 2, despite the formation of the Al_7Cu_2Fe phase. Consequently, the higher supersaturation level of the Al matrix phase led to the formation of highly concentrated nano-precipitates in the T6 sample. Meanwhile, the dislocation density was significantly decreased.

Therefore, the high hardness of the AB sample could mainly be attributed to a high dislocation density and to solid solution strengthening. The hardness could be further improved after an ageing heat treatment inducing an additional precipitation strengthening effect, compensating for the decrease in matrix strength by solute strengthening. The hardness of the ST and T6 samples was mainly governed by solid solution and precipitation strengthening, respectively. Considering the alloying content in the Al matrix as presented in Table 2, a total amount of 12.9 and 17.0 wt% η' precipitates with average particle size of 6 and 5 nm give a hardness increment of 54 and 76 HV for the DA and T6 sample, respectively. Hence, performing a solution heat treatment on the L-PBF-processed Al-Zn-Mg-Cu-based alloy is beneficial for a higher strength. It should be noted that the hardness increment calculated based on EDS results is semi-quantitative, but it facilitates the comparison of the strengthening effects between DA and T6 samples.

FOR THE PUBLISHED MANUSCRIPT, PLEASE VISIT ***ADDITIVE MANUFACTURING***: HTTPS://DOI.ORG/10.1016/J.ADDMA.2023.103460

Table 2. Average fraction of Zn, Mg, and Cu in the Al matrix and the grain boundary eutectic phase in the TiB_2/Al-Zn-Mg-Cu composite under DA, and ST condition.

Sample	Region	Zn (wt%)	Mg (wt%)	Cu (wt%)	Total content (wt%)
DA	Al matrix	4.9 ± 0.7	1.1 ± 0.2	6.9 ± 0.7	12.9 ± 0.4
	Eutectic phases	21.1 ± 1.8	3.9 ± 1.0	12.3 ± 0.4	37.2 ± 0.4
ST	Al matrix	8.2 ± 0.1	2.1 ± 0.1	6.7 ± 0.5	17.0 ± 0.5
T6	Al matrix	6.6 ± 0.3	1.7 ± 0.1	13.9 ± 2.2	22.2 ± 2.3

5. Conclusions

In the present work, a TiB_2/Al-Zn-Mg-Cu composite was successfully manufactured using L-PBF from a gas-atomized composite powder synthesized using an in-situ mixed salt method. A commercially available gas-atomized Al7075 powder was used as a reference material. The effects of reinforcing particles on the processability during L-PBF processing and on the precipitation behavior during direct-ageing (DA), solution treatment (ST), and T6 heat treatments were studied. The following main conclusions could be summarized,

- The unmodified Al-Zn-Mg-Cu alloy (Al7075) encountered a severe hot cracking problem during the L-PBF process, resulting in a volume fraction of 3.3 ± 0.7% of hot cracks in the as-built sample. The L-PBF-processed TiB_2/Al-Zn-Mg-Cu composite is crack-free, resulting in a relative density of 99.7 ± 0.1%.
- In contrast to the coarse columnar microstructure with strong (001) texture along the building direction in the Al-Zn-Mg-Cu alloy, the L-PBF-processed TiB_2/Al-Zn-Mg-Cu composite has an isotropic microstructure, consisting of fine equiaxed grains with submicrometer- and nanometer-sized TiB_2 particles distributed both within the FCC Al grains matrix and at the grain boundaries, as well as Zn, Mg, Cu, and Fe-rich eutectic phases, located in the interdendritic regions. The Al/TiB_2 interface is semi-coherent. The rapid solidification during L-PBF enabled the formation of a unique microstructure with a high dislocation density in the Al matrix, thermal mismatch dislocations in the vicinity of the TiB_2 particles, and refined grains with an average size of 2.0 ± 0.9 μm in the TiB_2/Al-Zn-Mg-Cu composite.
- The TiB_2/Al-Zn-Mg-Cu composite shows superior hardness values compared to the Al-Zn-Mg-Cu alloy under all the heat treatment conditions. The as-built TiB_2/Al-Zn-Mg-Cu composite showed a hardness of 163 ± 6 HV, significantly higher than 97 ± 7 HV of the as-built Al-Zn-Mg-Cu alloy. The increase in hardness is mainly attributed to a combination of grain refinement, Orowan strengthening, thermal mismatch, and load-bearing strengthening mechanisms due to the presence of TiB_2 nanoparticles, the elimination of hot cracks, and the strengthening effect from an excessive amount of alloying elements. The TiB_2 particles were thermally stable during heat treatments.
- The presence of fully coherent GP zones/early-stage η' precipitates and semi-coherent η' precipitates was observed in both DA and T6 TiB_2/Al-Zn-Mg-Cu samples. After a direct-ageing (DA) heat treatment, the interdendritic segregation and the high dislocation density were preserved, both originating from the L-PBF process. The precipitates were distributed non-uniformly in the DA sample. The smaller precipitates had either a platelet morphology with a width and length of 2-4 nm and around 10 nm, respectively, or a plate-like morphology with a diameter around 6 nm. The smaller precipitates were distributed in the Al matrix, while the

FOR THE PUBLISHED MANUSCRIPT, PLEASE VISIT ***ADDITIVE MANUFACTURING***: HTTPS://DOI.ORG/10.1016/J.ADDMA.2023.103460

larger precipitates were preferentially formed on the dislocations, exhibiting a width of 5-6 nm and a length around 13 nm for the platelets, or around 13 nm in diameter for the plate-like ones. Consequently, the hardness of the as-built TiB_2/Al-Zn-Mg-Cu composite increased from 163 ± 6 to 200 ± 5 HV after a DA heat treatment.

- A solution heat treatment enabled the dissolution of the interdendritic segregation and a precipitate-free matrix with an increased supersaturation level was obtained, while accompanied by a decrease in dislocation density and the formation of needle-shaped Al_7Cu_2Fe phase of around 0.14 ± 0.03 μm in width and 1.11 ± 0.43 μm in length. Subsequently, the T6 sample obtained a homogeneous Al grain matrix containing a high-density of well-dispersed precipitates. The platelets showed a width of 2-3 nm, a length of around 6 nm, and the plate-like precipitates showed a diameter of 4-5 nm. The hardness of the as-built TiB_2/Al-Zn-Mg-Cu composite increased to 171 ± 3 and 215 ± 2 HV under ST and T6 condition, respectively.
- The TiB_2/Al-Zn-Mg-Cu composite showed accelerated precipitation kinetics due to multiple factors via: (a) the solute segregation at the TiB_2/Al interfaces, (b) heterogeneous nucleation on the TiB_2/Al interfaces, and on the thermal mismatch dislocations in the vicinity of TiB_2 particles, (c) the increased amount of high angle grain boundaries and incoherent Al_7Cu_2Fe/Al interfaces that facilitated a faster solute transport, as well as (d) the higher chemical driving force due to the excessive alloying content.

Acknowledgements

The China Scholarship Council (Grant No. 201706220083) is acknowledged for financial support. The authors gratefully acknowledge the Hercules Foundation for project AKUL/1319 (CombiS(T)EM). The authors would like to acknowledge Prof. BrechtVan Hooreweder, Dr. Louca Goossens, and Ir. Yannis Kinds for the support on the L-PBF experiments using the 3D Systems Prox DMP 200 machine.

References

[1] E. MacDonald, R. Wicker, Multiprocess 3D printing for increasing component functionality, Science (80-.). 353 (2016) aaf2093–aaf2093. doi:10.1126/science.aaf2093.

[2] T. DebRoy, H.L. Wei, J.S. Zuback, T. Mukherjee, J.W. Elmer, J.O. Milewski, A.M. Beese, A. Wilson-Heid, A. De, W. Zhang, Additive manufacturing of metallic components – Process, structure and properties, Prog. Mater. Sci. 92 (2018) 112–224. doi:10.1016/j.pmatsci.2017.10.001.

[3] C. de Formanoir, U. Paggi, T. Colebrants, L. Thijs, G. Li, K. Vanmeensel, B. Van Hooreweder, Increasing the productivity of laser powder bed fusion: Influence of the hull-bulk strategy on part quality, microstructure and mechanical performance of Ti-6Al-4V, Addit. Manuf. 33 (2020). doi:10.1016/j.addma.2020.101129.

[4] G. Li, E. Brodu, J. Soete, H. Wei, T. Liu, T. Yang, W. Liao, K. Vanmeensel, Exploiting the rapid solidification potential of laser powder bed fusion in high strength and crack-free Al-Cu-Mg-Mn-Zr alloys, Addit. Manuf. 47 (2021) 102210. doi:10.1016/j.addma.2021.102210.

[5] Q. Jia, F. Zhang, P. Rometsch, J. Li, J. Mata, M. Weyland, L. Bourgeois, M. Sui, X. Wu, Precipitation kinetics, microstructure evolution and mechanical behavior of a developed Al–Mn–Sc alloy fabricated by selective laser melting, Acta Mater. 193 (2020) 239–251. doi:10.1016/j.actamat.2020.04.015.

[6] A. Iveković, M.L. Montero-Sistiaga, J. Vleugels, J.P. Kruth, K. Vanmeensel, Crack mitigation in Laser Powder Bed Fusion processed Hastelloy X using a combined numerical-experimental approach, J. Alloys Compd. 864 (2021) 158803. doi:10.1016/j.jallcom.2021.158803.

[7] N.T. Aboulkhair, M. Simonelli, L. Parry, I. Ashcroft, C. Tuck, R. Hague, 3D printing of Aluminium alloys: Additive Manufacturing of Aluminium alloys using selective laser melting, Prog. Mater. Sci. 106 (2019) 100578. doi:10.1016/j.pmatsci.2019.100578.

[8] J. Zhang, B. Song, Q. Wei, D. Bourell, Y. Shi, A review of selective laser melting of aluminum alloys: Processing, microstructure, property and developing trends, J. Mater. Sci. Technol. 35 (2019) 270–284.

doi:10.1016/j.jmst.2018.09.004.
[9] G. Li, S.D. Jadhav, A. Martín, M.L. Montero-Sistiaga, J. Soete, M.S. Sebastian, C.M. Cepeda-Jiménez, K. Vanmeensel, Investigation of Solidification and Precipitation Behavior of Si-Modified 7075 Aluminum Alloy Fabricated by Laser-Based Powder Bed Fusion, Metall. Mater. Trans. A Phys. Metall. Mater. Sci. 52 (2021) 194–210. doi:10.1007/s11661-020-06073-9.
[10] H. Zhao, F. De Geuser, A. Kwiatkowski da Silva, A. Szczepaniak, B. Gault, D. Ponge, D. Raabe, Segregation assisted grain boundary precipitation in a model Al-Zn-Mg-Cu alloy, Acta Mater. 156 (2018) 318–329. doi:10.1016/j.actamat.2018.07.003.
[11] S.D. Jadhav, P.P. Dhekne, S. Dadbakhsh, J.P. Kruth, J. Van Humbeeck, K. Vanmeensel, Surface Modified Copper Alloy Powder for Reliable Laser-based Additive Manufacturing, Addit. Manuf. 35 (2020). doi:10.1016/j.addma.2020.101418.
[12] S.D. Jadhav, P.P. Dhekne, E. Brodu, B. Van Hooreweder, S. Dadbakhsh, J.-P.P. Kruth, J. Van Humbeeck, K. Vanmeensel, Laser powder bed fusion additive manufacturing of highly conductive parts made of optically absorptive carburized CuCr1 powder, Mater. Des. 198 (2021) 109369. doi:10.1016/j.matdes.2020.109369.
[13] M.L. Montero-Sistiaga, Z. Liu, L. Bautmans, S. Nardone, G. Ji, J.P. Kruth, J. Van Humbeeck, K. Vanmeensel, Effect of temperature on the microstructure and tensile properties of micro-crack free hastelloy X produced by selective laser melting, Addit. Manuf. 31 (2020) 100995. doi:10.1016/j.addma.2019.100995.
[14] T. DebRoy, T. Mukherjee, H.L. Wei, J.W. Elmer, J.O. Milewski, Metallurgy, mechanistic models and machine learning in metal printing, Nat. Rev. Mater. 6 (2021) 48–68. doi:10.1038/s41578-020-00236-1.
[15] G. Wang, H. Ouyang, C. Fan, Q. Guo, Z. Li, W. Yan, Z. Li, The origin of high-density dislocations in additively manufactured metals, Mater. Res. Lett. 8 (2020) 283–290. doi:10.1080/21663831.2020.1751739.
[16] P. Rometsch, Q. Jia, K. V. Yang, X. Wu, Aluminum alloys for selective laser melting - towards improved performance, Elsevier Inc., 2019. doi:10.1016/B978-0-12-814062-8.00016-9.
[17] A. Aversa, G. Marchese, A. Saboori, E. Bassini, D. Manfredi, S. Biamino, D. Ugues, P. Fino, M. Lombardi, New aluminum alloys specifically designed for laser powder bed fusion: A review, Materials (Basel). 12 (2019) 1007. doi:10.3390/ma12071007.
[18] Q. Li, G. Li, X. Lin, D. Zhu, J. Jiang, S. Shi, F. Liu, W. Huang, K. Vanmeensel, Development of a high strength Zr/Sc/Hf-modified Al-Mn-Mg alloy using Laser Powder Bed Fusion: Design of a heterogeneous microstructure incorporating synergistic multiple strengthening mechanisms, Addit. Manuf. 57 (2022) 102967. doi:10.1016/j.addma.2022.102967.
[19] J. Zhang, J. Gao, B. Song, L. Zhang, C. Han, C. Cai, K. Zhou, Y. Shi, A novel crack-free Ti-modified Al-Cu-Mg alloy designed for selective laser melting, Addit. Manuf. 38 (2021) 101829. doi:10.1016/j.addma.2020.101829.
[20] J.H. Martin, B.D. Yahata, J.M. Hundley, J.A. Mayer, T.A. Schaedler, T.M. Pollock, 3D printing of high-strength aluminium alloys, Nature. 549 (2017) 365–369. doi:10.1038/nature23894.
[21] X.P. Li, G. Ji, Z. Chen, A. Addad, Y. Wu, H.W. Wang, J. Vleugels, J. Van Humbeeck, J.P. Kruth, Selective laser melting of nano-TiB 2 decorated AlSi10Mg alloy with high fracture strength and ductility, Acta Mater. 129 (2017) 183–193. doi:10.1016/j.actamat.2017.02.062.
[22] M.H. Ghoncheh, M. Sanjari, A.S. Zoeram, E. Cyr, B.S. Amirkhiz, A. Lloyd, M. Haghshenas, M. Mohammadi, On the microstructure and solidification behavior of new generation additively manufactured Al-Cu-Mg-Ag-Ti-B alloys, Addit. Manuf. 37 (2021) 101724. doi:10.1016/j.addma.2020.101724.
[23] D. Gu, Laser Additive Manufacturing of High-Performance Materials, Springer Berlin Heidelberg, Berlin, Heidelberg, 2015. doi:10.1007/978-3-662-46089-4.
[24] C. Gao, Z. Wang, Z. Xiao, D. You, K. Wong, A.H. Akbarzadeh, Selective laser melting of TiN nanoparticle-reinforced AlSi10Mg composite: Microstructural, interfacial, and mechanical properties, J. Mater. Process. Technol. 281 (2020) 116618. doi:10.1016/j.jmatprotec.2020.116618.
[25] Q. Tan, J. Zhang, N. Mo, Z. Fan, Y. Yin, M. Bermingham, Y. Liu, H. Huang, M.X. Zhang, A novel method to 3D-print fine-grained AlSi10Mg alloy with isotropic properties via inoculation with LaB6 nanoparticles, Addit. Manuf. 32 (2020) 101034. doi:10.1016/j.addma.2019.101034.
[26] T. Gao, S. Zhang, G. Liu, Q. Sun, J. Liu, Q. Sun, J. Sun, Z. Wang, X. Liu, X. Wang, A high strength AlSi10Mg alloy fabricated by laser powder bed fusion with addition of Al Ti C B master alloy powders, Materialia. 16 (2021) 101103. doi:10.1016/j.mtla.2021.101103.
[27] Z. Wang, C. Li, H. Wang, X. Zhu, M. Wu, J. Li, Q. Jiang, Aging Behavior of Nano-SiC/2014Al Composite Fabricated by Powder Metallurgy and Hot Extrusion Techniques, J. Mater. Sci. Technol. 32 (2016) 1008–1012. doi:10.1016/j.jmst.2016.07.011.
[28] M. Strangwood, C.A. Hippsley, J.J. Lewandowski, Segregation to SiC/Al interfaces in Al based metal matrix composites, Scr. Metall. Mater. 24 (1990) 1483–1487.
[29] Y. Ma, A. Addad, G. Ji, M.X. Zhang, W. Lefebvre, Z. Chen, V. Ji, Atomic-scale investigation of the interface precipitation in a TiB2 nanoparticles reinforced Al–Zn–Mg–Cu matrix composite, Acta Mater. 185 (2020) 287–

299. doi:10.1016/j.actamat.2019.11.068.
[30] C. Wu, K. Ma, D. Zhang, J. Wu, S. Xiong, G. Luo, J. Zhang, F. Chen, Q. Shen, L. Zhang, E.J. Lavernia, Precipitation phenomena in Al-Zn-Mg alloy matrix composites reinforced with B4C particles, Sci. Rep. 7 (2017) 1–11. doi:10.1038/s41598-017-10291-4.
[31] Y.T. Zhou, Y.N. Zan, S.J. Zheng, Q.Z. Wang, B.L. Xiao, X.L. Ma, Z.Y. Ma, Distribution of the microalloying element Cu in B4C-reinforced 6061Al composites, J. Alloys Compd. 728 (2017) 112–117. doi:10.1016/j.jallcom.2017.08.273.
[32] J. Lu, Y. Song, L. Hua, K. Zheng, D. Dai, Thermal deformation behavior and processing maps of 7075 aluminum alloy sheet based on isothermal uniaxial tensile tests, J. Alloys Compd. 767 (2018) 856–869. doi:10.1016/j.jallcom.2018.07.173.
[33] S. Gorsse, C. Hutchinson, M. Gouné, R. Banerjee, Additive manufacturing of metals: a brief review of the characteristic microstructures and properties of steels, Ti-6Al-4V and high-entropy alloys, Sci. Technol. Adv. Mater. 18 (2017) 584–610. doi:10.1080/14686996.2017.1361305.
[34] M. Chen, X. Li, G. Ji, Y. Wu, Z. Chen, W. Baekelant, K. Vanmeensel, H. Wang, J.-P.P. Kruth, Novel composite powders with uniform TiB2 nano-particle distribution for 3D printing, Appl. Sci. 7 (2017) 250. doi:10.3390/app7030250.
[35] M. Schaffer, B. Schaffer, Q. Ramasse, Sample preparation for atomic-resolution STEM at low voltages by FIB, Ultramicroscopy. 114 (2012) 62–71. doi:10.1016/j.ultramic.2012.01.005.
[36] Y. Xu, D. Casari, R.H. Mathiesen, Y. Li, Revealing the heterogeneous nucleation behavior of equiaxed grains of inoculated Al alloys during directional solidification, Acta Mater. 149 (2018) 312–325. doi:10.1016/j.actamat.2018.02.058.
[37] W. Kurz, D.J. Fisher, Fundamentals of solidification - Fourth revised Edition, Trans Tech Publ. Uetikon-Zuerich, Switz. (1998) 316.
[38] M. Sheikhi, F. Malek Ghaini, H. Assadi, Prediction of solidification cracking in pulsed laser welding of 2024 aluminum alloy, Acta Mater. 82 (2015) 491–502. doi:10.1016/j.actamat.2014.09.002.
[39] J.C. Lippold, Welding Metallurgy and Weldability, Weld. Metall. Weldability. 9781118230 (2014) 1–400. doi:10.1002/9781118960332.
[40] A. Chouhan, M. Hesselmann, A. Toenjes, L. Mädler, N. Ellendt, Numerical modelling of in-situ alloying of Al and Cu using the laser powder bed fusion process: A study on the effect of energy density and remelting on deposited track homogeneity, Addit. Manuf. 59 (2022) 103179. doi:10.1016/j.addma.2022.103179.
[41] P. Ma, C. Liu, Q. Chen, Q. Wang, L. Zhan, J. Li, Natural-ageing-enhanced precipitation near grain boundaries in high-strength aluminum alloy, J. Mater. Sci. Technol. 46 (2020) 107–113. doi:10.1016/j.jmst.2019.11.035.
[42] B. Cai, B.L. Adams, T.W. Nelson, Relation between precipitate-free zone width and grain boundary type in 7075-T7 Al alloy, Acta Mater. 55 (2007) 1543–1553. doi:10.1016/j.actamat.2006.10.015.
[43] H. Chen, J. Lu, Y. Kong, K. Li, T. Yang, A. Meingast, M. Yang, Q. Lu, Y. Du, Atomic scale investigation of the crystal structure and interfaces of the B′ precipitate in Al-Mg-Si alloys, Acta Mater. 185 (2020) 193–203. doi:10.1016/j.actamat.2019.11.059.
[44] J. Buha, R.N. Lumley, A.G. Crosky, Secondary ageing in an aluminium alloy 7050, Mater. Sci. Eng. A. 492 (2008) 1–10. doi:10.1016/j.msea.2008.02.039.
[45] J.A. Österreicher, G. Kirov, S.S.A. Gerstl, E. Mukeli, F. Grabner, M. Kumar, Stabilization of 7xxx aluminium alloys, J. Alloys Compd. 740 (2018) 167–173. doi:10.1016/j.jallcom.2018.01.003.
[46] X.J. Jiang, B. Noble, V. Hansen, J. Tafto, Influence of zirconium and copper on the early stages of aging in Al-Zn-Mg alloys, Metall. Mater. Trans. A. 32 (2001) 1063–1073. doi:10.1007/s11661-001-0117-7.
[47] A. Chemin, D. Marques, L. Bisanha, A. de J. Motheo, W.W. Bose Filho, C.O.F. Ruchert, Influence of Al7Cu2Fe intermetallic particles on the localized corrosion of high strength aluminum alloys, Mater. Des. 53 (2014) 118–123. doi:10.1016/j.matdes.2013.07.003.
[48] M. Wang, D. Chen, Z. Chen, Y. Wu, F. Wang, N. Ma, H. Wang, Mechanical properties of in-situ TiB2/A356 composites, Mater. Sci. Eng. A. 590 (2014) 246–254. doi:10.1016/j.msea.2013.10.021.
[49] G. Li, X. Huang, H. Wei, T. Liu, K. Vanmeensel, Laser Powder Bed Fusion of a Novel Cu-Modified AlSi10Mg Alloy : Processing , Microstructure , and Properties, Euro PM2020 Virtual Congr. (2020) 1–6.
[50] L. Lin, Z. Liu, W. Liu, Y. Zhou, T. Huang, Effects of Ag Addition on Precipitation and Fatigue Crack Propagation Behavior of a Medium-Strength Al–Zn–Mg Alloy, J. Mater. Sci. Technol. 34 (2018) 534–540. doi:10.1016/j.jmst.2016.11.008.
[51] Q. Tan, J. Zhang, Q. Sun, Z. Fan, G. Li, Y. Yin, Y. Liu, M.X. Zhang, Inoculation treatment of an additively manufactured 2024 aluminium alloy with titanium nanoparticles, Acta Mater. 196 (2020) 1–16. doi:10.1016/j.actamat.2020.06.026.
[52] T. Boellinghaus, J.C. Lippold, C.E.C. Editors, Cracking Phenomena in Welds IV, Springer International Publishing, Cham, 2016. doi:10.1007/978-3-319-28434-7.

[53] D. Gosslar, R. Günther, C. Hartig, R. Bormann, M. Zollinger, I. Steinbach, Grain refinement of γ-TiAl alloys by inoculation, Mater. Res. Soc. Symp. Proc. 1128 (2009) 91–96. doi:10.1557/proc-1128-u03-02.
[54] D.G. Eskin, L. Katgerman, A quest for a new hot tearing criterion, Metall. Mater. Trans. A Phys. Metall. Mater. Sci. 38 A (2007) 1511–1519. doi:10.1007/s11661-007-9169-7.
[55] M. Saadati, A.K. Edalat Nobarzad, M. Jahazi, On the hot cracking of HSLA steel welds: Role of epitaxial growth and HAZ grain size, J. Manuf. Process. 41 (2019) 242–251. doi:10.1016/j.jmapro.2019.03.032.
[56] M. Rappaz, J.M. Drezet, M. Gremaud, A new hot-tearing criterion, Metall. Mater. Trans. A Phys. Metall. Mater. Sci. 30 (1999) 449–455. doi:10.1007/s11661-999-0334-z.
[57] S. Kou, A criterion for cracking during solidification, Acta Mater. 88 (2015) 366–374. doi:10.1016/j.actamat.2015.01.034.
[58] A. Prasad, L. Yuan, P. Lee, M. Patel, D. Qiu, M. Easton, D. StJohn, Towards understanding grain nucleation under Additive Manufacturing solidification conditions, Acta Mater. 195 (2020) 392–403. doi:10.1016/j.actamat.2020.05.012.
[59] M.J. Bermingham, D.H. StJohn, J. Krynen, S. Tedman-Jones, M.S. Dargusch, Promoting the columnar to equiaxed transition and grain refinement of titanium alloys during additive manufacturing, Acta Mater. 168 (2019) 261–274. doi:10.1016/j.actamat.2019.02.020.
[60] S. Kou, Welding Metallurgy, John Wiley & Sons, Inc, 2002. doi:10.1002/0471434027.
[61] P. Schumacher, A.L. Greer, J. Worth, P. V. Evans, M.A. Kearns, P. Fisher, A.H. Green, New studies of nucleation mechanisms in aluminium alloys: Implications for grain refinement practice, Mater. Sci. Technol. 14 (1998) 394–404. doi:10.1179/mst.1998.14.5.394.
[62] D. Wearing, A.P. Horsfield, W. Xu, P.D. Lee, Which wets TiB2 inoculant particles: Al or Al3Ti?, J. Alloys Compd. 664 (2016) 460–468. doi:10.1016/j.jallcom.2015.12.203.
[63] A.M. Bunn, P. Schumacher, M.A. Kearns, C.B. Boothroyd, A.L. Greer, Grain refinement by Al-Ti-B alloys in aluminium melts: A study of the mechanisms of poisoning by zirconium, Mater. Sci. Technol. 15 (1999) 1115–1123. doi:10.1179/026708399101505158.
[64] M. Easton, D. Stjohn, Grain refinement of aluminum alloys: Part I. The nucleant and solute paradigms - a review of the literature, Metall. Mater. Trans. A Phys. Metall. Mater. Sci. 30 (1999) 1613–1623. doi:10.1007/s11661-999-0098-5.
[65] D. Turnbull, B. Vonnegut, Nucleation Catalysis., Ind. Eng. Chem. 44 (1952) 1292–1298. doi:10.1021/ie50510a031.
[66] J.H. Martin, B. Yahata, J. Mayer, R. Mone, E. Stonkevitch, J. Miller, M.R. O'Masta, T. Schaedler, J. Hundley, P. Callahan, T. Pollock, Grain refinement mechanisms in additively manufactured nano-functionalized aluminum, Acta Mater. 200 (2020) 1022–1037. doi:10.1016/j.actamat.2020.09.043.
[67] M.X. Zhang, P.M. Kelly, M.A. Easton, J.A. Taylor, Crystallographic study of grain refinement in aluminum alloys using the edge-to-edge matching model, Acta Mater. 53 (2005) 1427–1438. doi:10.1016/j.actamat.2004.11.037.
[68] A.M. Mitrašinović, F.C. Robles Hernández, Determination of the growth restriction factor and grain size for aluminum alloys by a quasi-binary equivalent method, Mater. Sci. Eng. A. 540 (2012) 63–69. doi:10.1016/j.msea.2012.01.072.
[69] Y.J. Liang, X. Cheng, H.M. Wang, A new microsegregation model for rapid solidification multicomponent alloys and its application to single-crystal nickel-base superalloys of laser rapid directional solidification, Acta Mater. 118 (2016) 17–27. doi:10.1016/j.actamat.2016.07.008.
[70] G. Sha, L. Yao, X. Liao, S.P. Ringer, Z.C. Duan, T.G. Langdon, Segregation of solute elements at grain boundaries in an ultrafine grained Al-Zn-Mg-Cu alloy, Ultramicroscopy. 111 (2011) 500–505. doi:10.1016/j.ultramic.2010.11.013.
[71] P. Lejček, Grain Boundary Segregation in Metals, Springer Science & Business Media, 2010. doi:10.1007/978-3-642-12505-8_1.
[72] H. Jiang, R.G. Faulkner, Modelling of grain boundary segregation, precipitation and precipitate-free zones of high strength aluminium alloys - I. The model, Acta Mater. 44 (1996) 1857–1864. doi:10.1016/1359-6454(95)00317-7.
[73] X. Zhang, T. Hu, J.F. Rufner, T.B. LaGrange, G.H. Campbell, E.J. Lavernia, J.M. Schoenung, K. Van Benthem, Metal/ceramic interface structures and segregation behavior in aluminum-based composites, Acta Mater. 95 (2015) 254–263. doi:10.1016/j.actamat.2015.05.021.
[74] M. De Cicco, H. Konishi, G. Cao, H.S. Choi, L.-S. Turng, J.H. Perepezko, S. Kou, R. Lakes, X. Li, Strong, ductile magnesium-zinc nanocomposites, Metall. Mater. Trans. A. 40 (2009) 3038.
[75] K.E. Knipling, D.C. Dunand, D.N. Seidman, Nucleation and precipitation strengthening in dilute Al-Ti and Al-Zr alloys, Metall. Mater. Trans. A Phys. Metall. Mater. Sci. 38 (2007) 2552–2563. doi:10.1007/s11661-007-9283-6.
[76] Q. Jia, P. Rometsch, P. Kürnsteiner, Q. Chao, A. Huang, M. Weyland, L. Bourgeois, X. Wu, Selective laser

melting of a high strength Al Mn Sc alloy: Alloy design and strengthening mechanisms, Acta Mater. 171 (2019) 108–118. doi:10.1016/j.actamat.2019.04.014.
[77] R. Li, M. Wang, Z. Li, P. Cao, T. Yuan, H. Zhu, Developing a high-strength Al-Mg-Si-Sc-Zr alloy for selective laser melting: Crack-inhibiting and multiple strengthening mechanisms, Acta Mater. 193 (2020) 83–98. doi:10.1016/j.actamat.2020.03.060.
[78] R.G. Munro, Material Properties of Titanium Diboride, J. Res. Natl. Inst. Stand. Technol. 105 (2000) 709–720. doi:10.6028/jres.105.057.